Towards Mechanism-based Constitutive Modelling of $L1_2$ Crystal Plasticity

by

Yuan Yin

Bachelor of Science in Engineering Mechanics,
Tsinghua University, Beijing, China (2000)

Submitted to the Department of Mechanical Engineering
in partial fulfillment of the requirements for the degree of

Master of Science in Mechanical Engineering

at the

MASSACHUSETTS INSTITUTE OF TECHNOLOGY

June 2003

Author .....
Department of Mechanical Engineering
May 9, 2003

Certified by .....
David M. Parks
Professor of Mechanical Engineering
Thesis Supervisor

Accepted by .....
Ain A. Sonin
Chairman, Department Committee on Graduate Students

Towards Mechanism-based Constitutive Modelling of $L1_2$ Crystal Plasticity

by

Yuan Yin

Submitted to the Department of Mechanical Engineering
on May 9, 2003, in partial fulfillment of the
requirements for the degree of
Master of Science in Mechanical Engineering

Abstract

A single-crystal plasticity model of the $L1_2$ structure intermetallic compound Ni_3Al is developed, in light of recent theoretical developments and experimental evidence. Computational results show that the model is capable of predicting the major anomalous mechanical behaviors of $L1_2$ structures, including increase of yield strength with increasing temperature, strong orientation dependence of the yield stress, tension-compression asymmetry, and small strain rate sensitivity.

Some ideas on revising the plasticity model have been presented. Though not completed, the new approach points to promising future directions in simulating both the yield behavior and the strain hardening properties of $L1_2$ compounds.

Thesis Supervisor: David M. Parks
Title: Professor of Mechanical Engineering

Acknowledgments

I begin by thanking my thesis supervisor, Professor David Parks, for his support over the last three years. He gave me the opportunity to work on an interesting and challenging problem and to learn the knowledge which will help me well in my profession.

It has been a great pleasure and privilege to share an office with a very interesting group of people who have been great friends as well as good sources of discussion: Adam Mulliken, Athanasios Arsenlis, Cheng Su, Hang Qi, Jin Yi, Mats Danielsson, Mike King, Nicoli Ames, Nuo Sheng, Rajdeep Sharma, Scott Therkelsen, Theodora Tzianetopoulou, Vaibhaw Vishal and Yujie Wei.

Thanks to Mr. Raymond Hardin, who was always very encouraging and helped with all information necessary to make things run smoothly.

Finally, many, many thanks to my family. Special mention must be made of my mom, Shu Liu, who was always there supporting me and encouraging me even in a very bad health condition herself. My husband, Qin, thanks for your understanding and being so supportive to me.

Contents

List of Figures

List of Tables

Chapter 1

Introduction

Nickel-based superalloys are of great interest because of their excellent mechanical properties of high-temperature strength and creep resistance. Based on these particular mechanical properties, they are subjected to very severe operating conditions in commercial and military applications, especially in gas turbine engines. The yield and tensile strengths of nickel-based superalloys are also fundamental design parameters in the manufacture of aerospace components.

Nickel-based superalloys have very complex microstructures, an fcc Ni-base solid solution matrix (the γ phase) hardened by suitable solutes and the $\gamma\prime$ precipitates. Thus their outstanding high-temperature strength is derived from a combination of several principal strengthening mechanisms. Consequently, there are a large number of variables that can influence the overall mechanical behaviors of these superalloys, which make them very difficult to design. Quantitative models can be very useful in this respect, assisting the development of new alloys and guiding the implementation of existing alloys.

Many factors should be included in the modeling network. The emphasis of this thesis was put on plasticity modeling and application of the primary γ' precipitates.

The basic composition of the γ' precipitates is Ni_3Al with $L1_2$ crystal structure, which is a derivative of the fcc crystal structure. It is typical of compounds of composition AB_3 with the minority (A) atoms occupying the corner sites and the majority (B) atoms occupying the face centers, as shown in Figure 1-1. As a result, the lattice

translation vector in $L1_2$ compounds is $< 110 >$ as opposed to $1/2 < 110 >$ in fcc materials.

The $L1_2$ compounds have been studied extensively since the 1950s, owing to their low density, moderate ductility at room temperature, and, especially, their anomalous mechanical behaviors. In this chapter, the most important characteristics of the anomalous yield behaviors, the key microscopic structures, the main microscopic observations and the distinguished existing theories will be outlined.

1.1 Characteristics of the anomalous regime

The first demonstration of the unusual mechanical behavior of alloys having the $L1_2$ ordered structure was provided by Westbrook [1957], who showed that there is a peak in the hardness vs. temperature dependence of Ni_3Al, Figure 1-2(a). A later study [Flinn, 1960] confirmed from tensile testing that the 0.01% offset yield strength of polycrystalline Ni_3Al also increases with temperature, Figure 2-1(b). Since then, the experimental work devoted to this phenomenon is very extensive, and the yield anomaly has also been reported in $L1_2$ compounds other than Ni_3Al and in two-phase nickel-based γ/γ' superalloys [Allan, 1995].

The most important characteristics of the anomalous yield behavior are summarized by the following ([Vitek and Pope, 1996]):

1. The yield and /or flow stress increases with temperature, both in tension and compression, until a peak temperature is reached. This phenomenon is commonly referred to as the anomalous behaviour of the $L1_2$ ordered structure. Above the peak temperature, ($T_p \cong 800 - 1200K$ for Ni_3Al), the strength drops off significantly.

2. The peak temperature is also the boundary across which the dominant active slip system changes from $\{111\} < 101 >$ to $\{001\} < 101 >$ [Staton-Bevan and Rawlings, 1975].

3. The yield stress anomaly largely disappears in the micro-strain range. The

yield stress is nearly independent of temperature for an offset strain smaller than $\sim 10^{-5}$, while the anomaly is fully developed for the offset strain $\cong 10^{-3}$ (Figure 1-3). [Thornton, 1970; Mulford and Pope, 1973]

4. The Schmid law is violated: crystal orientations with the same Schmid factor (e.g., $< 001 >$ and $< 011 >$) have different yield strengths under uniaxial states of stress. The strong orientation dependence of the critical resolved shear stress (CRSS) [Takeuchi and Kuramoto, 1971, 1973] (Figure 1-4) and the remarkable tension-compression yield asymmetry [Lall, 1979; Ezz *et al.*, 1982] (Figure 1-5) show that non-glide components of the stress tensor (the "non-Schmid" stress components) play an important role.

5. The work hardening rate also exhibits an unusual behavior in the anomalous regime. At strains $\cong 1.5\%$, "the work-hardening rate first increases with increasing temperature, reaches a peak at temperatures close to half of T_p and then decreases with increasing temperature" [Staton-Bevan, 1983]. While, in the low-strain region (plastic strain less than 0.2%), the work-hardening rate increases steadily with temperature up to T_p [Ezz and Hirsch, 1995].

6. The strain-rate dependence of the yield stress is positive but very small below the peak temperature. Commonly, $\Delta\tau/\tau \leq 1\%$ for strain-rate changes by a factor of ten. [Thornton *et al.*, 1970]. However, above the peak temperature, a strong positive strain-rate sensitivity is observed [Umakoshi *et al.*, 1984].

1.2 Superlattice dislocations, Planar faults and superkinks

Most of the unusual mechanical properties of the $L1_2$ structure compound mentioned in the last section are controlled by the material's unique micro-structures. A review of some major microscopic observations will be presented in the next section. In order to have a good understanding of these observations, it is appropriate to give

descriptions of some basic micro-features first.

1.2.1 Superlattice dislocations

The total dislocation Burgers vector in the $L1_2$ crystal structure is $< 110 >$, since it must be a lattice translation vector. Dislocations having such long Burgers vectors are commonly called superdislocations. Superdislocations often dissociate into partial dislocations, which are usually termed "superpartial dislocations" or simply "superpartials". When the superpartials separate, a planar fault is created on their plane of spreading. If the fault energy is sufficiently low, unpaired or very widely separated superpartials are sometimes seen. However, the more usual case is for some combination of superpartials to move together as a group, the leading dislocation(s) creating local disorder along planar faults and the trailing dislocation(s) correcting the disorder, as show in Figure 1-6.

1.2.2 Planar Faults

1. Antiphase boundaries (APBs) : APBs can exist on any planes; for $L1_2$ structure, the most important planes are $\{111\}$ and $\{010\}$. When the superdislocation $< 110 >$ dissociates into two $\frac{1}{2} < 110 >$ superpartials, an APB is created in between, and separates the two partial dislocations, as shown in Figure 1-6. Figure 1-7 provides another way of visualizing this fault. In Figure 1-7 (a), three successive (111) planes are shown by large, medium, and small circles, representing atoms in the upper, middle, and lower planes, respectively. Open and closed circles represent majority (A) and minority (B) atoms, respectively. Considering shifting the top layer and all those above it by $\frac{1}{2}[\bar{1}01]$, shown as $\vec{b}_A$ in Figure 1-7(b), a single-layer fault is created in which the stacking sequence is still locally fcc, but there are now B-B nearest neighbors (marked by the dashed lines), where none exist in the unfaulted material.

2. Complex Stacking Faults (CSF): The complexity of the dislocations structures in the $L1_2$ ordered intermetallic compounds goes beyond that of the simple

splitting into two superpartials. The further splitting of the superpartials (e.g., each $\frac{1}{2} < 110 >$ dislocation splitting into two $\frac{1}{6} < 112 >$ Shockley partials) on $\{111\}$ is known to play an important role in influencing the motion of superdislocations and the properties of plastic flow. The complex stacking fault (CSF) which is generated in between the two Shockley partials stands for a complex stacking fault which involves not just a disruption in the stacking sequence but also changes in the bonding between the atoms across the fault. The formation of a CSF can be schematically shown in Figure 1-7 (d). The top (111) layer and all above it shift relative to those below it by $\frac{1}{6}[\bar{1}12]$, such that the B atoms in the top layer lie directly above the A atoms in the bottom layer. This shift results in a local hcp stacking with nearest neighbor violations, as shown by the dotted lines. The CSF fault is expected to have a higher energy than the APB on $\{111\}$ planes.

3. Superlattice Intrinsic Stacking Faults (SISF) : In some cases the APB does not represent the major mode of dissociation, and faults of other types dominate the coupling of the partials. In $L1_2$ crystal structure, another possible mode of dissociation for the $< 110 > \{111\}$ superdislocations involves splitting into two super-lattice Shockley partials $\frac{1}{3} < 112 >$, which bound the superlattice intrinsic stacking fault (SISF). Schematically shown in Figure 1-7 (c), SISF is produced by shifting the top layer and all those above it by $\frac{1}{3}[\bar{2}11]$. The local stacking sequence becomes hcp as in the CSF, but there are no nearest neighbor violations. An SISF is expected to be of rather lower energy than APBs.

1.2.3 Superkinks

As mentioned above, $\{111\} < 101 >$ is the dominant slip system below the peak temperature. The $< 101 >$ superdislocations dissociate on the $\{111\}$ plane into two APB-coupled superpartials. Due to the lower APB energy on the $\{001\}$ plane and the great elastic asymmetry, the screw-oriented dislocations would cross-slip from the $\{111\}$ plane to the $\{001\}$ cube plane. The cross-slip procedure is complicated, and

the fulfillment may contain different sequences.

Simply speaking, when the leading superpartial cross-slips onto the cube plane, it can dissociate into two CSF-coupled Shockleys either on the (111) plane or on the octahedral cross-slip plane $(1\bar{1}1)$, depending on the how large the cross-slip step is. The latter case is a sessile configuration, and thus the dislocation is immobilized. For the former case, the two superpartials may both cross-slip for several times until they reach a final sessile configuration. For both of these two immobile cases, the screw superpartials cross-slipped onto the (100) planes, and the APB also spreads on the cube cross-slip plane; this configuration is the so-called Kear-Wilsdorf (K-W) lock [Kear and Wilsdorf, 1962]. Figure 1-8 schematically illustrates the formation of a K-W type lock.

Because of the cross-slip, the screw dislocations dominating the substructure of $L1_2$ compounds observed in the anomalous region are not perfectly straight, but contain many steps, which lie in the (111) slip plane (see also in section 1.3 below). These steps are mobile segments far from screw orientation, joining adjacent screw segments which have advanced by different distances. Since these steps are not constrained to the periodicity of the lattice and can be quite long, they have been termed "superkinks" [Sun and Hazzledine, 1988].

1.3 Microscopic observations in $L1_2$ Compounds

Extensive microscopic observations have been made, giving indications of many dislocation mechanisms. A review of microscopic observations has been made by Veyssiere [1989], and those which are commonly considered to be important in explaining the origin of the yield stress anomaly are briefly listed below.

1. Most of the dislocations observed in the anomalous region are long $< 101 >$ screws [Kear and Hornbecher, 1966; Staton-Bevan and Rawlings, 1975], which indicates that screw dislocations are much less mobile than the non-screws, as confirmed later by several in-situ deformation experiments [Nemoto *et al.*, 1977;

Lours *et al.*, 1991]. The sessile screw superdislocation segments are mostly locked by the Kear-Wilsdorf configuration.

2. The dominating long screws are not straight but contain many steps (superkinks), which have been observed post-mortem. Superkinks could be classified into three categories according to the way they connect the screw segments: "regular kinks on superdislocations, switched-over kinks reversing the order of superpartials, and simple kinks affecting one superpartial only" [Saada *et al.*, 1993]. A decrease of the superkink's heights has been observed with both increasing temperature and increasing stress, by statistical methods. The mean height of superkinks measured by Couret, Sun and Hirsch [1993] in Ni_3Ga and by Bontemps [1991] in $Ni_3(Al, Hf)$ varies from 18-20 nm at 300 K to 10-12nm at 673 K. Similar measurements performed by Dimiduk [1989] indicate that the height of the superkinks varies inversely to the strength of the alloys.

3. Dislocation cross-slip and gliding in the cube plane have been observed in the higher-temperature range of the yield stress anomaly [Molenat *et al.*, 1993; Molenat and Caillard, 1994]. Cube slip is also reported by Lall [1979] for directions near $< 111 >$ in this temperature range. Post-mortem observations in Ni_3Ga [Molenat *et al.*, 1993] and in-situ observations in Ni_3Al [Molenat and Caillard, 1994] indicate that the reverse cross-slip process from cube onto octahedral planes also operates at high temperatures.

4. In-situ observations in Ni_3Al show that straight screw dislocations move in a jerky way. In the lower temperature range of the stress anomaly, the dissociated superpartials in the octahedral plane jump over distances often scaling with their dissociation width. In the higher temperature range of the yield stress anomaly, "octahedral glide proceeds by bursts with indications of double cross-slip between octahedral and cube planes" [Molenat and Caillard, 1994]. All dislocations are dissociated in cube planes just after the bursts.

1.4 Existing theories of Deformation in $L1_2$ Structures

The $L1_2$ nickel aluminide Ni_3Al has been studied extensively since the 1950s. Since the discovery of the anomalous temperature dependence of the yield stress in Ni_3Al, a number of reasons for this phenomenon have been put forward.

Explanations were first based on changes in long-range order, because the anomalous yield behavior in β-brass is related to such changes [Brown, 1959]. However, Ni_3Al remains ordered up to melting, and therefore changes in order cannot explain the phenomenon [Vitek and Pope, 1996].

A series of models based on the assumption that individual dislocations carrying the plastic deformation change their splitting and/or core structure in response to changes in temperature were then brought forward. The first such suggestion was made by Flinn. He hypothesized that "at high temperatures, dislocations originally gliding on (111) planes, climb into (001) planes and thus become immobile" [Flinn, 1960]. This transition is considered to be driven by the reduction of the anti-phase boundary (APB) energy, and is responsible for the formation of Kear-Wilsdorf locks

The assumption of the cross-slip of screw dislocations is, indeed, substantiated by abundant experimental observations. Hence, the cross-slip-induced immobilization of the screws becomes a preferential concept, and many recent quantitative models of the yield anomaly in $L1_2$ compounds are grounded on this idea. The first such model was proposed by Takeuchi and Kuramoto [Takeuchi and Kuramoto, 1973], who suggested that:

> "The increase of the yield stress is proportional to the density of the dislocation segments that have cross-slipped into the (001) plane and which then provide local pinning points that hinder the motion of the rest of the dislocations. The production of such pinning points is thermally activated, and the pinning mechanism was considered to be due to the change of the core configuration."

This model was then significantly advanced by Paidar, Pope and Vitek (the PPV model), who demonstrated that "the observed orientation dependence of the yield stress is a natural consequence of the pinning transformations of screw dislocations" [Paidar *et al.*, 1984].

The PPV model is a "dynamical break-away" model. Dislocations with Burgers vector $[\bar{1}01]$ in essentially screw orientations move on a (111) plane. Occasionally a short segment cross-slips onto the (010) plane, where it forms an immobile barrier to movement of the rest of the dislocation. The screw dislocation is assumed to break away from this local pinning point when the unlocked segments have advanced by a critical distance d_c, and a new pinning point is formed along a length l (Figure 1-9).

Cross-slip to the (010) planes is thought to be driven by both the lowering of APB energy and non-radial elastic interactions [Vitek and Pope, 1996]. The locking process of a small cross-slip segment is considered to be caused by the core transformation mechanism of Takeuchi and Kuramoto's model. Thus an estimation of the energy cost for the core transformation leads to the calculation of the activation enthalpy for the locking process. The critical value of the resolved shear stress, τ, in the (111) glide plane is given by:

$$\tau = \tau_o \exp(-\frac{H_l}{3kT}), \tag{1.1}$$

where τ_o is a constant, k is the Boltzmann constant, T is the absolute temperature, and H_l is the locking enthalpy. The locking enthalpy deduced in the PPV model involves non-Schmid shear stress components, and is able to give reasonable explanations for the dependence of the yield strength on crystal orientation and the tension and compression asymmetry. Thus, the cross-slip process described in the PPV model has been widely accepted and the PPV-type activation enthalpy is inherited by many following works.

The idea of point obstacles is followed by Cuitino and Ortiz [1993]. They proposed that: "yield and hardening are presumed to be the effect of point obstacles opposing the motion of dislocations". The sources of the point obstacles for the octahedral slip system are considered to come from both "forest dislocations" and "cross-slip

pinning". The density of point obstacles of the latter type is proportional to the activation enthalpy deduced by the PPV model. Christine Allan [1995], also put forward a similar model in which the slip resistances of the octahedral system are enhanced by a parameter proportional to the PPV-type cross-slip activation enthalpy.

But in reality, the assumption of local cross-slip pinning is not consistent with the widely-observed extended Kear-Wilsdorf type locks. And the PPV model failed to explain the small strain-rate effects. The problem is: based on the nature of point obstacles, no unlocking effects are included into the average screw dislocation velocity.

These inconsistencies have led to an alternate picture of flow in which near-screw character dislocations are assumed to propagate by the lateral, kink-like motion of the mixed segments between the KW locks. Among these, Hirsch's superkink model [Hirsch, 1992] is one of the most successful.

Contrary to the PPV model, Hirsch considered that the superkinks formed on the screws can move rapidly along the dislocation, forming a long length of screw segment cross-slipped on (010). The screw dislocation segments are then locked by edge dipole barriers or by Kear-Wilsdorf type locks. These barriers can be unlocked by the movement of edge-character superkinks through a thermally-activated mechanism which has a large athermal component. In simulation of the locking process, Hirsch applied the same locking enthalpy given by the PPV model; thus this model can explain the dependence of the yield strength on crystal orientation and asymmetry of the yield strength for tension and compression, as PPV did. As for unlocking, since it is also considered to be a thermally activated process, the average dislocation velocity of the screw dislocation is slowed down by the waiting time before unlocking can occur. And by adding a large athermal component to the unlocking enthalpy, a small overall strain-rate sensitivity can be derived.

These latest models, particularly that of Hirsch, which will be described in detail in Chapter 2, can explain most features of the yield strength in a manner consistent with the microstructure, including the small strain-rate sensitivity. Figure 1-9 (a) schematically shows the PPV break-through model and Hirsch's superkink model.

Though successful in explaining most of the anomalous yield behavior, both the

PPV model and Hirsch's superkink model have some limitations. From Figure 1-9 (a), we particularly notice that in both models, the obstacles are distributed periodically, and no changes in the obstacle density and the average segment advance distance (the average superkink height in Hirsch's model) are allowed for a given dislocation. Hence, the assumed immobile "pinned phase" and the assumed mobile "unpinned phase", are actually two steady-state phases of dislocation motion. The CRSS is, then, the stress demarcating the boundary between the pinned and unpinned dynamical phases on the primary slip plane. For constant strain-rate simulation, such an assumption leads to a non-hardening prediction after the yield point, as shown in Figure 1-9 (b). In contrast, for constant strain-rate tests, extraordinarily large rates of strain hardening (up to $\mu/10$, where μ is the shear modulus) are observed until just below the peak temperature [Thornton *et al.*, 1970]. This inconsistency forces one to reconsider the "steady-state" assumption implicit in both the PPV and Hirsch models.

Another superkink-based model that needs to be mentioned here is the ELU (extended-locking/unlocking) model proposed by Louchet [1995]. The basic idea is: In order to overcome the resistance force acted on the ends of the superkink, superkinks need to have a height longer than a critical value l_p to be mobile; on the other hand, long superkinks with height longer than another critical value, l_m, tend to bounce out and generate new superkinks. Without a clear definition, Louchet assumed that once the superkink is mobile, the superkink velocity is independent of its height. He further proposed that to maintain a constant applied strain rate, the density of mobile superkinks must remain unchanged. Thus, the exhaustion and multiplication of mobile dislocations need to be balanced, and hereby the yield stress anomaly is reached.

Motivated by the idea of "exhaustion of dislocations", which was proposed by Mills and Chrzan [1992] and Louchet [1995], the Hirsch superkink model has been revised. The basic idea is:

The net mobility of a screw dislocation is related to the average height of the superkinks on it. In this way, mobile dislocations do not simply remain mobile for all time, but will experience "exhaustion of mobility" if their average kink height falls

below a critical value. The mobile dislocation density and the evolution of the kink height are taken to be dependent on each other and related to temperature and the applied stress.

Coupling this idea with Hirsch's superkink unlocking model, the revised dynamic model then inherits all of its successful parts in predicting the yield behavior of $L1_2$ compounds. Moreover, it also shows a promising direction for simulating the high strain hardening rate of this material.

1.5 Outline of the Thesis

Chapter 1 has introduced characteristics of the anomalous region, the crystal structure and main microscopic observations in $L1_2$ compounds. A brief survey of existing models of deformation in $L1_2$ structures is also presented.

In Chapter 2, the single crystal constitutive framework is developed, and Hirsch's model is implemented into a finite element algorithm to investigate the main characteristics in the anomalous region of Ni_3Al. Successful predictions of the yield stress for different temperatures, different orientations and in both tension and compression, are presented and compared with experimental results.

In Chapter 3, basic ideas of a revised model are described. A reasonable prediction of high rate of strain hardening has been achieved. Discussions of this model and future improvements are also proposed.

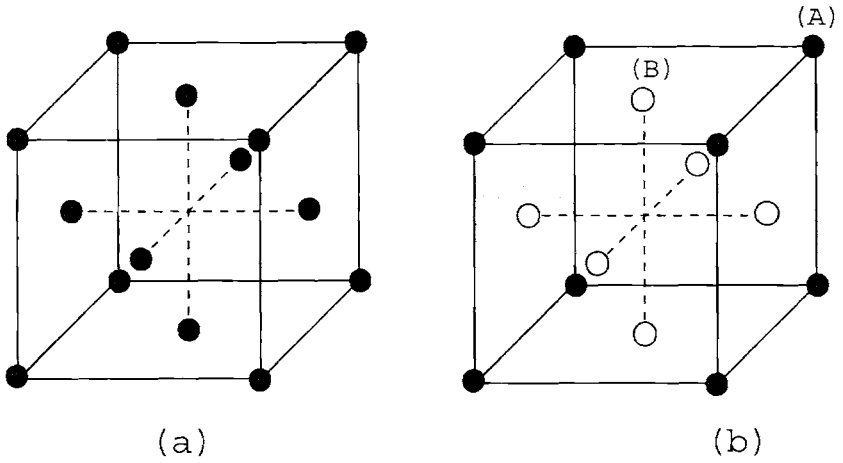

Figure 1-1: (a) The fcc unit cell and (b) the $L1_2$ unit cell of AB_3 compounds.

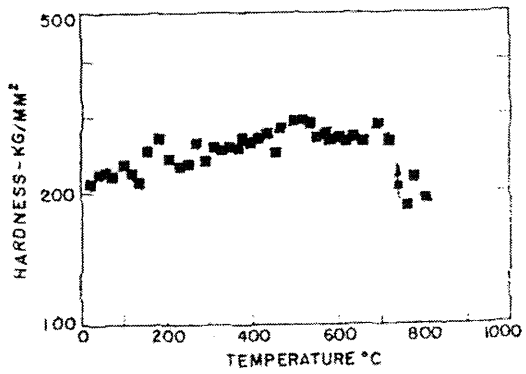

(a)

V. Vitek et al.

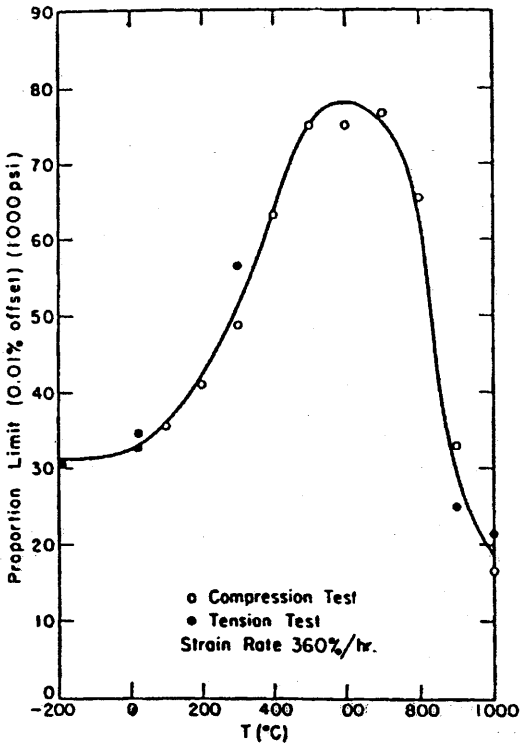

(b)

Figure 1-2: (a) Temperature dependence of the hardness of polycrystalline Ni_3Al [Westbrook, 1957]; (b) Flow stress of polycrystalline Ni_3Al as a function of temperature [Flinn, 1960].

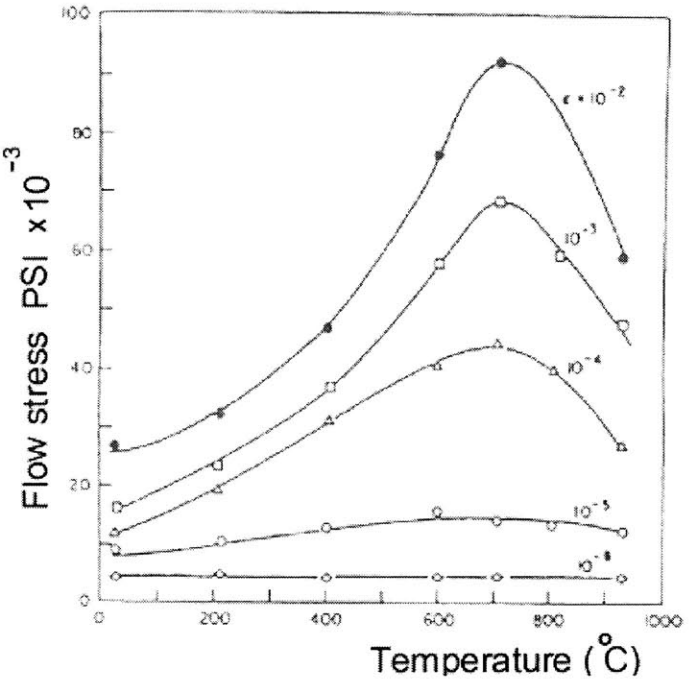

Figure 1-3: Dependence of the flow stress of Ni_3Al on temperature and plastic deformation offset. [Thornton, 1970].

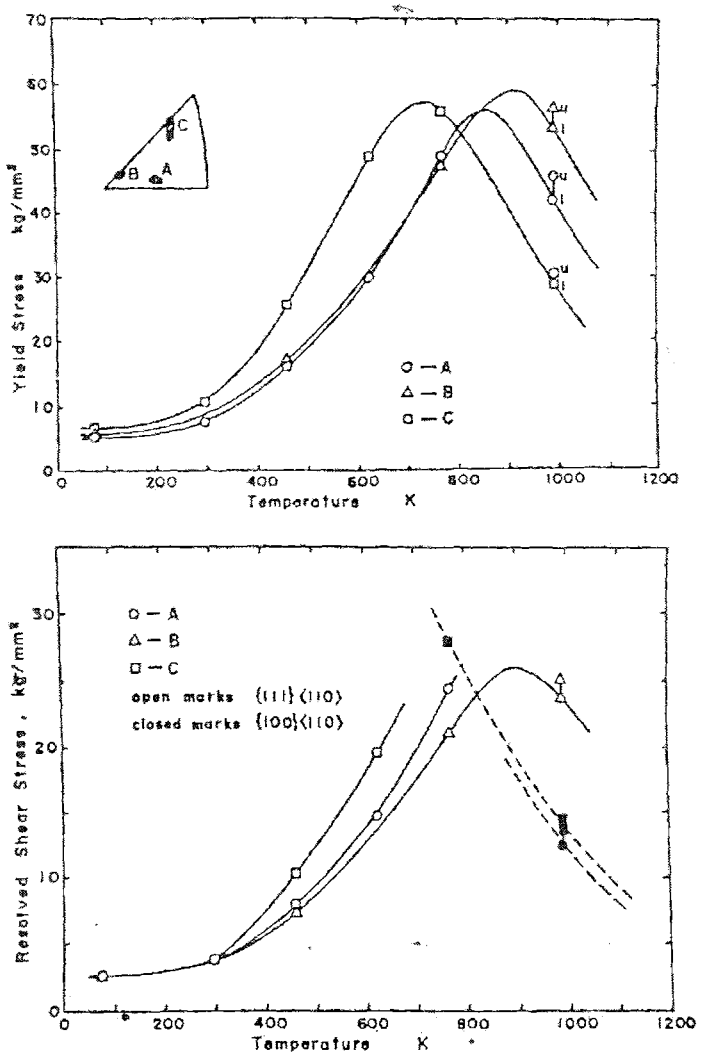

Figure 1-4: Uniaxial yield stress and CRSS for $(111)[\bar{1}0\bar{1}]$ and $(001)[1\bar{1}0]$ slip, in single crystal Ni_3Ga as functions of temperature and orientation of the tensile/compressive axis [Takeuchi and Kuramoto, 1973].

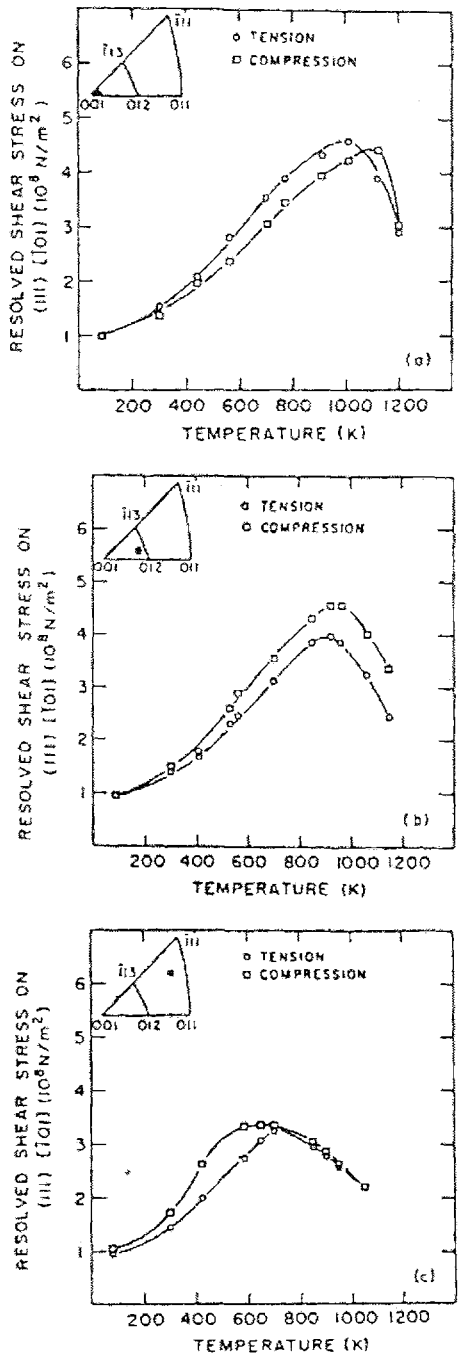

Figure 1-5: Temperature dependence of the CRSS for $(111)[\bar{1}0\bar{1}]$ slip, measured for $Ni_3(Al, Nb)$ in both tension and compression, for three different orientations of the tensile/compressive axis [Ezz *et al.*, 1982].

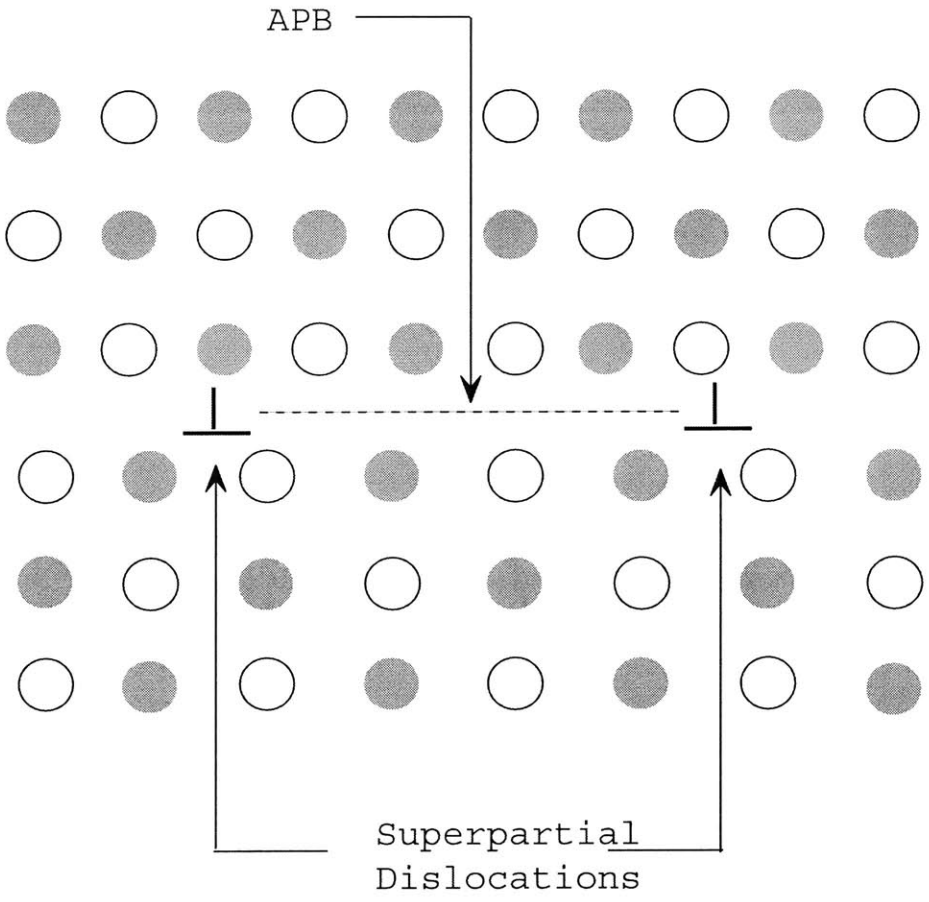

Figure 1-6: Two superpartial dislocations connected by a patch of antiphase boundary (APB) [Sun, 1995].

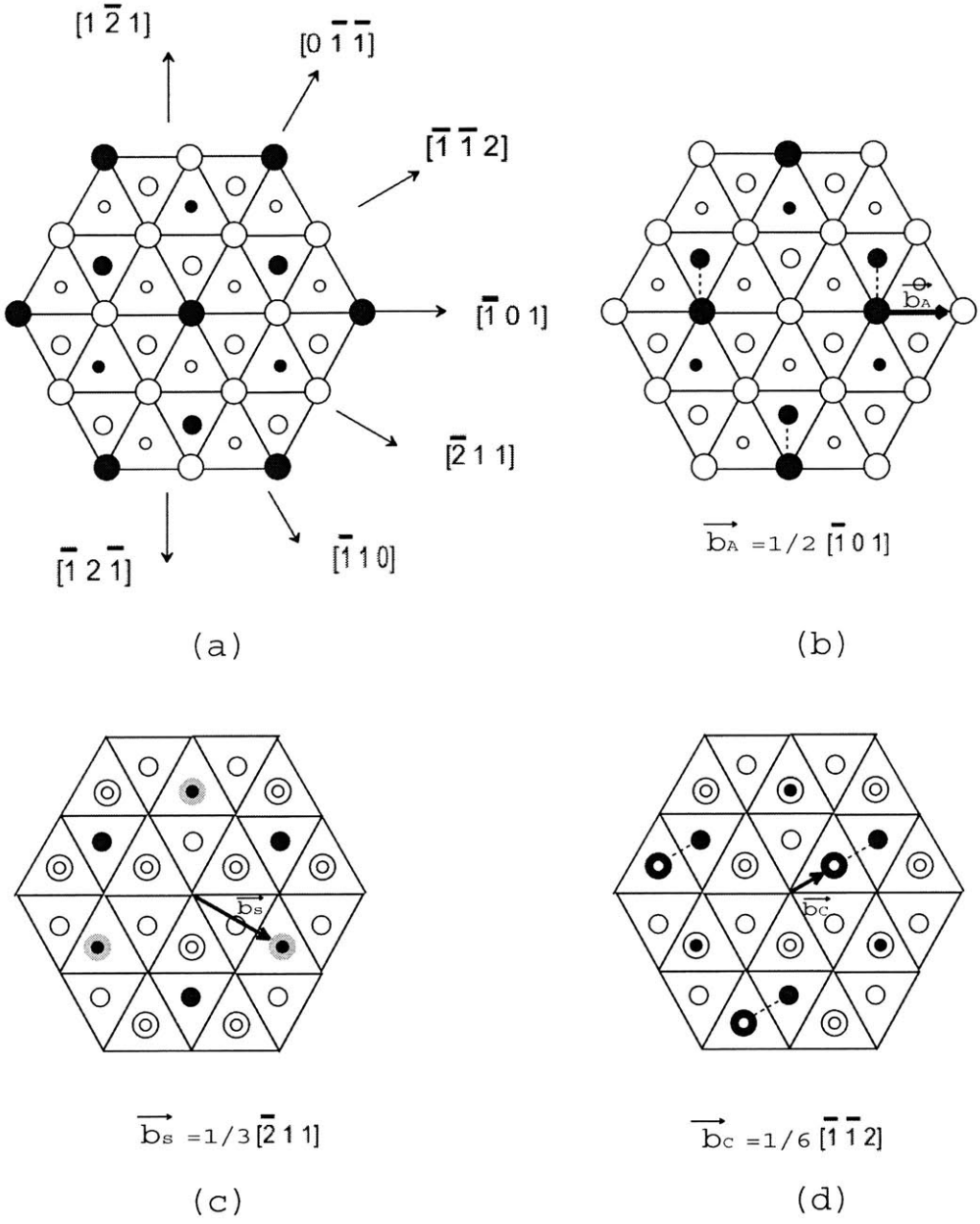

Figure 1-7: Three types of fault in an A_3B alloy with the $L1_2$ structure. (a) three (111) planes; (b)APB; (c)SISF (d) CSF [Liu and Pope, 1994].

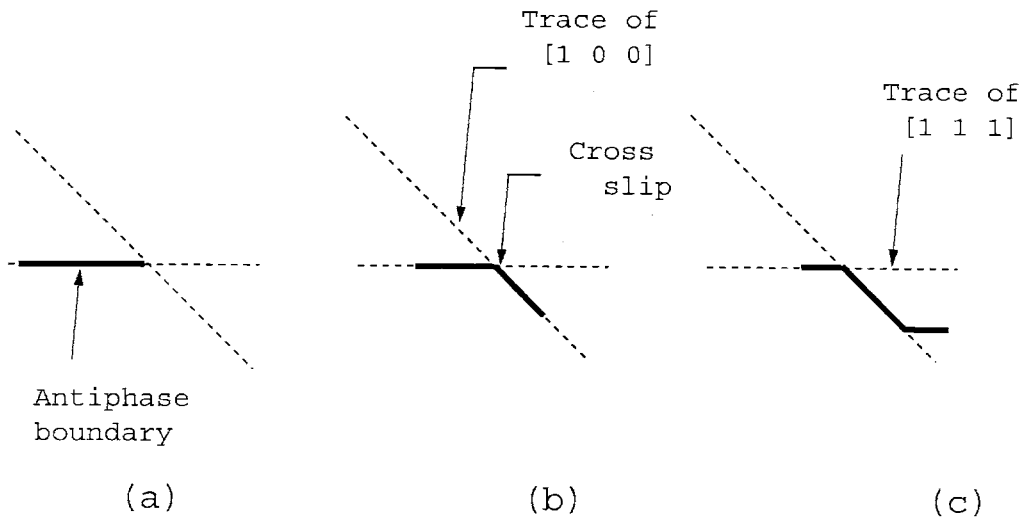

Figure 1-8: The Kear-Wilsdorf lock formed by cross-slip pinning. (a) A screw superdislocation dissociates into two superpartials on the [111] plane, bounding an APB in between; (b) The leading superpartial cross-slips to the [001] plane; (c) The formation of a Kear-Wilsdorf lock [Allan, 1995].

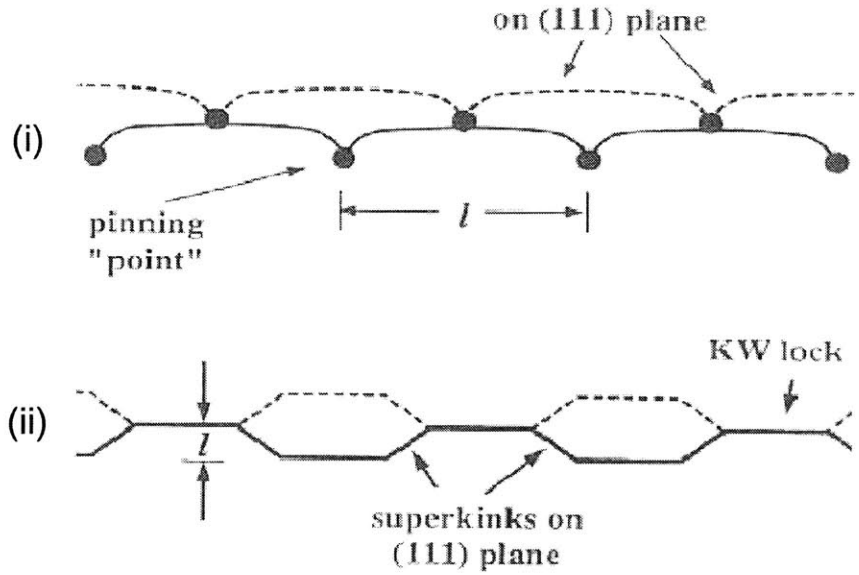

(a)

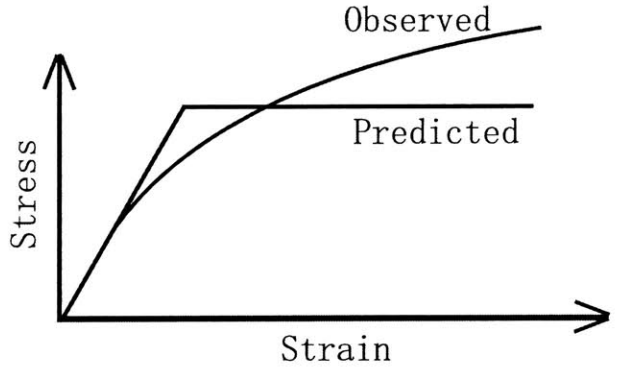

(b)

Figure 1-9: (a) Illustration of the successive positions for a dislocation moving on the (111) plane by (i) bowing between pinning points and (ii) by the lateral motion of superkinks; (b) Schematic comparison of the constant strain-strain test predicted from the "steady-state" models with typical experimental result. [Chrzan and Mills, 1996].

Chapter 2

Modeling of $L1_2$ Intermetallics – $\gamma\prime$ phase

2.1 Constitutive Model

The single-crystal kinematics described below is based on the developments of Asaro and Rice [1977]. The total deformation gradient, $\mathbf{F}$, mapping a reference configuration of the material to the final configuration, may be decomposed by the following form:

$$\mathbf{F} = \mathbf{F}^e\mathbf{F}^p, \tag{2.1}$$

where $\mathbf{F}^p$, the plastic deformation gradient, locally maps the original configuration to an intermediate configuration which describes the effects of plastic deformation on an unrotated and undeformed crystal lattice, and $det\ \mathbf{F}^p = 1$. The elastic deformation gradient, $\mathbf{F}^e$, maps the local intermediate configuration to the final deformed configuration, and is associated with small elastic stretches and arbitrary rigid-body rotations. The evolution equation for the plastic deformation gradient is given by the flow rule:

$$\dot{\mathbf{F}}^p = \mathbf{L}^p\mathbf{F}^p, \tag{2.2}$$

where $\mathbf{L}^p$ is the plastic flow rate. In crystals, $\mathbf{L}^p$ is comprised of the superposition of the resolved crystallographic plastic shear rates, $\dot{\gamma}^\alpha$, such that:

$$\mathbf{L}^p = \sum_\alpha \dot{\gamma}^\alpha \mathbf{m}_0^\alpha \otimes \mathbf{n}_0^\alpha, \tag{2.3}$$

where $\mathbf{m_0}^\alpha$ and $\mathbf{n}_0^\alpha$ are unit lattice vectors, defining the slip direction and the slip plane normal of the slip system α respectively, in a fixed reference configuration. The plastic shearing strain rate on each system, $\dot{\gamma}^\alpha$, is given by Orowan's equation:

$$\dot{\gamma^\alpha} = \rho_m^\alpha b \bar{v}^\alpha, \tag{2.4}$$

where ρ_m^α is the density of the mobile dislocations for slip system α, b is the magnitude of the Burgers vector, and $\bar{v}^\alpha$ is the average velocity of the mobile dislocations for slip system α.

During plastic deformation, the crystal lattice may elastically stretch and rotate. In the deformed configuration, the slip direction and slip plane normal, $\mathbf{m}_*^\alpha$ and $\mathbf{n}_*^\alpha$, are related to the initial lattice directions by the elastic deformation gradient:

$$\mathbf{m}_*^\alpha = \mathbf{F}^e \mathbf{m}_0^\alpha; \qquad \mathbf{n}_*^\alpha = \mathbf{F}^e \mathbf{n}_0^\alpha. \tag{2.5}$$

At given temperature, the constitutive equation for stress is given in terms of a linear elastic relation:

$$\bar{\mathbf{T}} = \mathcal{L}[\mathbf{E}^e], \tag{2.6}$$

where the elastic strain measure, $\mathbf{E}^e$, corresponding to the Cauchy-Green strain with respect to the intermediate configuration, is defined as:

$$\mathbf{E}^e \equiv \frac{1}{2}\left\{\mathbf{F}^{eT}\mathbf{F}^e - \mathbf{I}_2\right\}, \tag{2.7}$$

in which, $\mathbf{I}_2$ is the second-order identity tensor.

The work-conjugate stress measure in Eq. 2.6, $\bar{\mathbf{T}}$, corresponding to the second Piola-Kirchhoff stress with respect to the intermediate configuration, is related to

Cauchy stress, $\mathbf{T}$, through the following transformation:

$$\bar{\mathbf{T}} = \det(\mathbf{F}^e)\mathbf{F}^{e-1}\mathbf{T}\mathbf{F}^{e-\mathbf{T}}, \tag{2.8}$$

and $\mathcal{L}$ in Eq. 2.6 is the fourth-order anisotropic elasticity tensor.

2.2 Application of Hirsch's Model to Ni_3Al Single Crystals

2.2.1 Hirsch's model

Hirsch's model is based on a careful study of microstructural observations of $L1_2$ alloys. As mentioned in Chapter 1, one of the most significant microscopic observation in $L1_2$ compounds is the dominance of the long, straight, and less mobile screw superdislocations. The edge dislocations present themselves mainly as the links connecting the long screw dislocations and their cross-slipped parts. Hence, screw dislocations are chosen as the carriers of the plastic deformation in this model, though it is assumed that their motion is due to the mobile superkinks shuttling along them. The movement of the screws can be described by steadily switching between two dynamic phases: a locking phase for the formation of dislocation locks and an unlocking phase for the overcoming of those locks. The basic idea of Hirsch's model has been schematically shown in Figure 2-2 (a).

Formation of locks

Dislocations with the long $< 110 >$ Burgers vector in $L1_2$ order crystals usually dissociate into two superpartials, bounding an antiphase boundary (APB), with each of the superpartials further dissociating into two Shockley partials either on the original (111) plane or on the cross-slip $(1\bar{1}1)$ plane, bounding a complex stacking fault (CSF). This structure is shown schematically in Figure 2-1 (a). This dissociation mechanism is found for dislocations in Ni_3Al and Ni_3Ga in the yield stress anomaly region and

is considered to be associated with the anomalous behavior [Hirsch, 1992]. There is a driving force for the screws with this structure to cross-slip from (111) to (010). This arises partly from the lower APB energy on (010) [Flinn, 1960], and partly due to the elastic anisotropic interaction between the two screw superpartials [Yoo, 1986].

Following the PPV model, this cross-slip process can be described by a core-transformation mechanism (as shown in Figure 2-1(b)), which includes three steps: (i) Constriction of the glissile core on the (111) plane, (ii) movement of the constricted dislocation along the (010) plane, and (iii) further splitting of the cross-slipped superpartial on to the cross-slip $(1\bar{1}1)$ plane [Vitek and Pope, 1996].

The activation enthalpy H_l for the locking part, is then estimated by the energy cost of the core transformation process, and is explicitly given by PPV model as:

$$H_l = W_c + \frac{\mu b^3}{2\pi}\left\{\frac{c}{2} - \left[\frac{(\frac{\Delta E}{b^2} + \frac{|\tau_{cb}|}{2})\pi}{\mu}\right]^{1/2}\right\}, \tag{2.9}$$

where W_c is the constriction energy which is associated with steps (i) and (iii), and is explicitly expressed as:

$$W_c = \frac{\mu b^3}{2\pi}\left[h + \frac{\lambda}{\mu}(\tau_{pe} - \kappa\tau_{se})\right]. \tag{2.10}$$

In the above Eq. 2.9, c is the normalized self-energy of the kink, approximately equal to 0.5, and ΔE is the energy difference per unit length of the dislocation between the sessile and glissile core configurations shown in Figure 2-1(b) [Vitek and Pope, 1996]. In Eq. 2.10, h and λ are dimensionless constants depending on the width of the superpartial splitting in an unstressed solid. W_c should have a value of the order of $\sim 10^0$ ev, which makes the part inside the square brackets on the right side of Eq. 2.10 have the order of $\sim 10^0$. Assuming the two terms in the square brackets have same order, we find $h \sim 10^0$ and $\lambda \sim 10^2$. κ is also a dimensionless constant with magnitude less than one. τ_{cb}, τ_{pe} and τ_{se} are the non-Schmid stress components described by Figure 2-2(b).

τ_{cb} is the resolved shear stress component on the cross-slip (010) plane, in the

direction parallel to the total Burgers vector, and can be expressed as:

$$\tau_{cb}^{\alpha} \doteq (\bar{\mathbf{T}}) \cdot (\mathbf{m}_{cb}^{\alpha} \otimes \mathbf{n}_{cb}^{\alpha}), \tag{2.11}$$

where $\mathbf{n}_{cb}^{\alpha}$ is the unit vector defining the normal of the cross-slip (010) plane, and $\mathbf{m}_{cb}^{\alpha}$ is the unit vector in the direction of the total Burgers vector of the screw dilocation.

The resolved shear stress component in the primary (111) plane in the direction perpendicular to the total Burgers vector, τ_{pe}, is defined as:

$$\tau_{pe}^{\alpha} \doteq (\bar{\mathbf{T}}) \cdot (\mathbf{m}_{pe}^{\alpha} \otimes \mathbf{n}_{pe}^{\alpha}), \tag{2.12}$$

where $\mathbf{n}_{pe}^{\alpha}$ is the unit vector defining the normal of the primary (111) plane, and $\mathbf{m}_{pe}^{\alpha}$ is the unit vector in the direction perpendicular to the total Burgers vector.

Similarly, τ_{se}, the resolved shear stress component in the cross-slip $(1\bar{1}1)$ plane in the direction perpendicular to the total Burgers vector, is defined as:

$$\tau_{se}^{\alpha} \doteq (\bar{\mathbf{T}}) \cdot (\mathbf{m}_{se}^{\alpha} \otimes \mathbf{n}_{se}^{\alpha}), \tag{2.13}$$

where $\mathbf{n}_{se}^{\alpha}$ is the unit vector defining the normal of the cross-slip $(1\bar{1}1)$ plane, and $\mathbf{m}_{se}^{\alpha}$ is the unit vector in the direction perpendicular to the total Burgers vector. Table 2-2 contains, for each octahedral slip system, the planes and directions that define these shear stress components.

Introducing the non-Schmid stress components into the activation enthalpy H_l is very important in explaining the cross-slip process. The value of the constriction energy, W_c, differs if the sign of the applied stress changes, which contributes to the asymmetry of the CRSS in tension and compression; and the variation of the non-Schmid stress components with crystal orientation provides a good explanation for the property of strong orientation-dependence of CRSS in uniaxial stressing.

The basic difference between Hirsch's model and the PPV model is that cross-slip no longer happens locally ("point-wise") in the locking process, as in PPV. The pinning jogs formed on the screw by cross-slip can move rapidly along the screw

dislocation, forming a long length of screw segment on (010) planes. The long cross-slipped segments are then stabilized either by the formation of the well-known Kear-Wilsdorf locks or by edge dipole barriers. The formation process of an edge dipole barrier has been schematically shown in Figure 2-3.

Unlocking by superkinks

As mentioned in the above section, the screw dislocations are stabilized by two mechanisms, the dipole barrier locks and the K-W locks. These locks are considered to be much stronger than the point obstacles of the PPV model, and harder to unlock. Hence, in Hirsch's model, the unlocking process, which is thermally activated and involves a large athermal component, has the rate-controlling feature. The bypassing process of the dipole barriers by the movement of superkinks has been given schematically in Figure 2-4. Kear-Wilsdorf type locks are unlocked by a similar mechanism, controlled by a similar athermal stress, but with a larger activation energy.

The activation enthalpy for the unlocking process, H_u, is explicitly given by Hirsch for each slip system as:

$$H_u{}^{\alpha} = H_{u0} - (\tau^{\alpha} - \tau_g)V, \tag{2.14}$$

where H_{u0} is considered to be a constant with a value in the order of $\sim 10^0 ev$, τ_g is a temperature-independent deformation resistance, and V is the activation volume. τ_g is given as:

$$\tau_g = p\frac{\mu b}{l}, \tag{2.15}$$

and V is given as:

$$V = qll'_c b, \tag{2.16}$$

where p and q are dimensionless constants estimated to be 0.359 and 3.1, respectively [Hirsch, 1992]. By substituting these two definitions, Eq. 2.14 is rewritten in the following form:

$$H_u{}^{\alpha} = H_{u0} + 1.1\mu b^3\frac{l'_c}{b} - 3.1\tau^{\alpha}b^2\frac{l'_c}{b}l, \tag{2.17}$$

where μ is the shear modulus, l is the advance distance by the screw segment, which

is also the superkink height, as shown in Figure 2-2(a); b is the magnitude of the total Burgers vector, and l_c' is the critical length of superkink for cross-slip to occur, which is assumed to be equal to b . The resolved shear stress τ^α is defined by the applied stress and crystal geometry:

$$\tau^\alpha \doteq (\bar{\mathbf{T}}) \cdot (\mathbf{m}_0^\alpha \otimes \mathbf{n}_0^\alpha). \tag{2.18}$$

2.2.2 Selection of Discrete Dislocation Basis

The first step in modeling a crystalline material in this dislocation density framework is to choose a dislocation density discretization. The only active slip direction in the $L1_2$ order crystal is the close-packed $< 110 >$, except at very high temperatures (above $\sim 1100K$). In the anomalous regime where the flow stress is increasing with increasing temperature, slip occurs primarily on the $(111) < 110 >$ systems. At temperatures above the peak, slip occurs increasingly on $(100) < 110 >$ systems. Since the model will be applied to capture the plastic response of single-crystal Ni_3Al below the peak temperature ($T_p \sim 800K$), a total of twelve distinct screw dislocation densities which describe the $(111) < 110 >$ systems will be used. (Cube slip is also observed for orientations far from $< 001 >$, at relatively low temperatures in the anomalous yield region [Lall et al., 1979]. The model will be modified to account for this in future work.) The Burgers vectors, tangent line directions, and the slip plane normals are given in Table 2-1.

2.2.3 Selection of Constitutive Functions

In developing the internal modeling functions, each geometrically similar dislocation will have the same functional form and material constants for dislocation mobility. The mobile screw dislocation density is defined as a constant ($\rho_m \sim 10^{12}\ m^{-2}$ [Hirsch, 1992]), and the average velocity of screw dislocation is defined according to Hirsch's model:

$$\bar{v}_s^\alpha = v_{s0}\ exp\left\{\frac{-(H_u^\alpha - H_l^\alpha)}{kT}\right\}, \tag{2.19}$$

where the constant value of v_{s0} is estimated to be $10^6\ nm/s$, and the superscript α represents each different slip system. The locking and unlocking activation enthalpies for each slip-system have been given in the above section.

By applying the assumption that $l_c' \sim b$ [Hirsch, 1992] to the definition of the unlocking activation enthalpy, Eq. 2.17 can be simplified as:

$$H_u^\alpha \doteq H_{u0} + (\mu - 3.0\frac{l}{b}\tau^\alpha)b^3. \tag{2.20}$$

For the locking enthalpy, considering that $b^2|\tau_{cb}| \ll \Delta E$ and combining the constant parts, H_l can be rewritten as in the following way:

$$H_l^\alpha = b^3\left[C_1 + C_2(\tau_{pe}^\alpha - \kappa\tau_{se}^\alpha) + C_3|\tau_{cb}^\alpha|\right]. \tag{2.21}$$

Where the constants C_1, C_2 and C_3 are expressed as:

$$\begin{aligned} C_1 &= \frac{\mu}{2\pi}\left(h + \frac{c}{2} - \sqrt{\frac{\pi\Delta E}{\mu b^2}}\right); \\ C_2 &= \frac{\lambda}{2\pi}; \\ C_3 &= -\frac{1}{8}\sqrt{\frac{\mu b^2}{\Delta E}}. \end{aligned}$$

Thus the average velocity of the screw dislocation for each slip system can be written as:

$$\bar{v}_s^\alpha = v_{s0}^\alpha \exp\frac{-\left\{H_{u0}^{\alpha*} - 3.0\frac{l}{b}b^3\left[\tau^\alpha + \frac{C_2}{3.0\frac{l}{b}}(\tau_{pe}^\alpha - \kappa\tau_{se}^\alpha) + \frac{C_3}{3.0\frac{l}{b}}|\tau_{cb}^\alpha|\right]\right\}}{kT}, \tag{2.22}$$

where

$$H_{u0}^{\alpha*} = H_{u0}^\alpha + b^3(\mu - C_1). \tag{2.23}$$

2.2.4 Finite Element Implementation of Hirsch's Model

Hirsch's model for single crystal Ni_3Al was implemented into the commercially available FEM package ABAQUS/Standard as a user-defined material (UMAT), and was used with first-order brick (C3D8) elements to simulate the behavior of single crystal Ni_3Al subject to uniaxial tension and compression at different temperatures.

The ABAQUS/Standard UMAT is part of an implicit algorithm that enforces nodal equilibrium at every time increment. The inputs to the UMAT interface are the total deformation gradient at time t, $\mathbf{F}(t)$; the Cauchy stress at time t, $\mathbf{T}(t)$; an estimate of the total deformation gradient at time $t^* = t + \Delta t$, $\mathbf{F}(t^*)$; and a set of state-dependent variables at time t. The state-dependent variables in this formulation are the plastic strain rate, $\dot{\gamma}^\alpha$, and the plastic deformation gradient, $\mathbf{F}^p$, with respect to the reference configuration.

Given the input variables to the UMAT interface, the subroutine is responsible for calculating the Cauchy stress at time t^*, $\mathbf{T}(t^*)$; the plastic deformation gradient at time t^*, $\mathbf{F}^p(t^*)$; the material jacobian at time t^*, $\mathcal{C}(t^*)$; and update the state-dependent variables. The material jacobian is defined as:

$$\mathcal{C} \equiv \frac{\partial \mathbf{T}(t^*)}{\partial \mathbf{E}^t(t^*)}, \tag{2.24}$$

where $\mathbf{E}^t(t^*)$ is the relative strain tensor. It is defined by:

$$\mathbf{E}^t(t^*) \equiv ln(\mathbf{U}^t(t^*)), \tag{2.25}$$

where $\mathbf{U}^t(t^*)$ is the relative stretch tensor. The relative stretch tensor is evaluated from the polar decomposition of the relative deformation gradient, $\mathbf{F}^t(t^*)$, such that:

$$\mathbf{F}^t(t^*) = \mathbf{R}^t(t^*)\mathbf{U}^t(t^*). \tag{2.26}$$

The relative deformation gradient is determined by the following expression:

$$\mathbf{F}^t(t^*) = \mathbf{F}(t^*)\mathbf{F}^{-1}(t). \tag{2.27}$$

Time Integration Procedure

The determination of the state at time t^* from the inputs to the UMAT subroutine employs a backward Newton solving algorithm. This section will develop the relevant equations that are iterated to solve for the state at the new time increment.

If we combine the constitutive equation found in Eq. 2.6:

$$\bar{\mathbf{T}} = \mathcal{L}[\mathbf{E}^e],$$

with Eq. 2.7:

$$\mathbf{E}^e \equiv \frac{1}{2}\left\{\mathbf{F}^{eT}\mathbf{F}^e - \mathbf{I}_2\right\},$$

and Eq. 2.1:

$$\mathbf{F} = \mathbf{F}^e\mathbf{F}^p,$$

we can rewrite the constitutive equation into the following form:

$$\bar{\mathbf{T}}(t^*) = \frac{1}{2}\mathcal{L}\left\{\mathbf{F}^{p-T}(t^*)\mathbf{F}^T(t^*)\mathbf{F}(t^*)\mathbf{F}^{p-1}(t^*) - \mathbf{I}_2\right\}. \tag{2.28}$$

Assuming that $\mathbf{L^p}$ is constant over the time increment, time integration of the plastic flow rule in Eq. 2.2 leads to:

$$\mathbf{F}^p(t^*) = exp[\Delta t\mathbf{L}^p(t^*)]\mathbf{F}^p(t). \tag{2.29}$$

The time increments taken during the course of the deformation are typically small, allowing for the exponential in Eq. 2.29 to be approximated by a Taylor series to give:

$$\mathbf{F}^p(t^*) \doteq [\mathbf{I}_2 + \Delta t\mathbf{L}^p(t^*)]\mathbf{F}^p(t^*). \tag{2.30}$$

Inversion of Eq. 2.30 to the same level of accuracy with the substitution of the

crystallographic slip rates for the plastic velocity gradient from Eq. 2.3 leads to:

$$\mathbf{F}^{p-1}(t^*) \doteq \mathbf{F}^{p-1}(t)[\mathbf{I}_2 - \Delta t \sum_{\alpha} \dot{\gamma}^{\alpha}(t^*)\mathbf{S}^{\alpha}], \tag{2.31}$$

where

$$\mathbf{S}^{\alpha} = \mathbf{m}_0^{\alpha} \otimes \mathbf{n}_0^{\alpha}, \tag{2.32}$$

and by Eq. 2.4 and Eq. 2.19, the plastic shearing strain rate on each system is defined, at fixed temperature, as a function of applied stress:

$$\dot{\gamma}^{\alpha}(t^*) = \dot{\gamma}^{\alpha}(\bar{\mathbf{T}}(t^*)). \tag{2.33}$$

The crystallographic strain rates are also functions of the crystalline geometry, but for notational simplicity the geometry dependence is not explicitly included in this section. Substitution of Eq. 2.31 into Eq. 2.28 leads to the following relationship:

$$\bar{\mathbf{T}}(t^*) \doteq \bar{\mathbf{T}}^{tr} - \Delta t \sum_{\alpha} \dot{\gamma}^{\alpha}(\bar{\mathbf{T}}(t^*))\mathbf{C}^{\alpha}, \tag{2.34}$$

where

$$\bar{\mathbf{T}}^{tr} = \frac{1}{2}\mathcal{L}[\mathbf{B} - \mathbf{I}_2], \tag{2.35}$$

$$\mathbf{B} = \mathbf{F}^{p-T}(t)\mathbf{F}^{T}(t^*)\mathbf{F}(t^*)\mathbf{F}^{p-1}(t), \tag{2.36}$$

$$\mathbf{C}^{\alpha} = \frac{1}{2}\mathcal{L}[\mathbf{K}^{\alpha}], \tag{2.37}$$

and

$$\mathbf{K}^{\alpha} = \mathbf{B}\mathbf{S}^{\alpha} + \mathbf{S}^{\alpha T}\mathbf{B}. \tag{2.38}$$

All of the quantities in Eqs. 2.35 - 2.38 are known.

Equation 2.34 has $\bar{\mathbf{T}}(t^*)$ posed in such a way that it is a function of itself and known quantities. Therefore, they can be iteratively solved to find solution at the next time increment.

A column vector, $\mathbf{Z}$, is created by containing the second Piola-Kirchhoff stress tensor as a six-dimensional vector in the following manner:

$$\mathbf{Z} = \begin{bmatrix} \bar{\mathbf{T}}_{11}(t^*) \\ \bar{\mathbf{T}}_{22}(t^*) \\ \bar{\mathbf{T}}_{33}(t^*) \\ \bar{\mathbf{T}}_{12}(t^*) \\ \bar{\mathbf{T}}_{23}(t^*) \\ \bar{\mathbf{T}}_{31}(t^*) \end{bmatrix} = \begin{bmatrix} \bar{\mathbf{T}}_{1}(t^*) \\ \bar{\mathbf{T}}_{2}(t^*) \\ \bar{\mathbf{T}}_{3}(t^*) \\ \bar{\mathbf{T}}_{4}(t^*) \\ \bar{\mathbf{T}}_{5}(t^*) \\ \bar{\mathbf{T}}_{6}(t^*) \end{bmatrix} \tag{2.39}$$

The solution of the stress after the nth iteration of the Newton method is given by:

$$\mathbf{Z}_{n+1} = \mathbf{Z}_n - \mathcal{F}^{-1}[\mathbf{W}_n], \tag{2.40}$$

where

$$\mathbf{W}_n = \left[\bar{\mathbf{T}}_n(t^*) - \bar{\mathbf{T}}^{tr} + \Delta t \sum_\alpha \dot{\gamma}^\alpha(\bar{\mathbf{T}}_n(t^*))\mathbf{C}^\alpha\right], \tag{2.41}$$

and

$$\mathcal{F} = \mathcal{I} + \Delta t \left[\sum_\alpha \mathbf{C}^\alpha \otimes \frac{\partial \dot{\gamma}^\alpha(\bar{\mathbf{T}}_n(t^*))}{\partial \bar{\mathbf{T}}_n(t^*)}\right]. \tag{2.42}$$

Here $\mathcal{I}$ is 6 by 6 identity matrix. In Eq. 2.40 the $\mathbf{W}_n$ column vector has the same format as the $\mathbf{Z}$ vector, and in Eq. 2.41 the tensors $\bar{\mathbf{T}}_n$, and $\mathbf{C}^\alpha$ are written as column vectors also.

The initial guess of the stress at time t^* is done by the following procedure:

$$\bar{\mathbf{T}}_{n=0}(t^*) = \frac{1}{2}\mathcal{L}\left\{\mathbf{F}^{p-T}(t^*)^*\mathbf{F}^T(t^*)\mathbf{F}(t^*)\mathbf{F}^{p-1}(t^*)^* - \mathbf{I}_2\right\}, \tag{2.43}$$

where

$$\mathbf{F}^{p-1}(t^*)^* = \mathbf{F}^{p-1}(t)[\mathbf{I}_2 - \Delta t \sum_\alpha \dot{\gamma}^\alpha(t)\mathbf{S}^\alpha]. \tag{2.44}$$

After the iterative solution is found to converge to within a small tolerance for the set of non-linear equations, the state is updated. The plastic deformation gradient at time t^* is updated using Eq. 2.30, and the elastic deformation gradient is calculated

by using Eq. 2.1 and inverting the plastic deformation gradient. Once the elastic deformation gradient at time t^* is obtained, the Cauchy stress at time t^* is calculated through Eq. 2.8, and the crystallographic orientations are updated through Eq. 2.5.

Calculation of the Material Jacobian

For small changes in the deformation gradient over the time increment, the relationship between $\mathbf{E}^t(t^*)$ and $\mathbf{U}^t(t^*)$ can be approximated by:

$$\mathbf{E}^t(t^*) \doteq \mathbf{U}^t(t^*) - \mathbf{I}_2. \tag{2.45}$$

Differentiating this equation, the following result is obtained:

$$d\mathbf{E}^t(t^*) \doteq d\mathbf{U}^t(t^*). \tag{2.46}$$

Therefore, the material jacobian can be approximated by:

$$\mathcal{C} \doteq \frac{\partial \mathbf{T}(t^*)}{\partial \mathbf{U}^t(t^*)}. \tag{2.47}$$

For simplicity, indicial notation will be used to develop the equations associated with the derivation of the material jacobian. Inversion of Eq. 2.8 takes the form:

$$T_{ij} = [det(\mathbf{F}^e)]^{-1}(F^e_{im}\bar{T}_{mn}F^e_{jn}). \tag{2.48}$$

Taking the partial derivative of the Cauchy stress with respect to the relative stretch tensor leads to

$$\begin{aligned}\frac{\partial T_{ij}}{\partial U^t_{kl}} &= [det(\mathbf{F}^e)]^{-1}[\mathcal{S}_{imkl}\bar{T}_{mn}F^e_{jn} + F^e_{im}\mathcal{Q}_{mnkl}F^e_{jn} + \\ &\quad F^e_{im}\bar{T}_{mn}\mathcal{S}_{jnkl} - F^e_{im}\bar{T}_{mn}F^e_{jn}(F^{e-1}_{qp}\mathcal{S}_{pqkl})],\end{aligned} \tag{2.49}$$

where

$$\mathcal{S}_{ijkl} \equiv \frac{\partial F^e_{ij}}{U^t_{kl}}, \tag{2.50}$$

and

$$\mathcal{Q}_{ijkl} \equiv \frac{\partial \bar{T}_{ij}}{U^t_{kl}}. \tag{2.51}$$

From a combination of Eqs. 2.1, 2.26, 2.27 and 2.31, the elastic deformation is approximated by the following expression:

$$F^e_{ij}(t^*) \doteq R^t_{ik}(t^*)U^t_{kl}(t^*)F^e_{lm}(t)[\delta_{mj} - \sum_\alpha \dot{\gamma}^\alpha(t^*)\Delta t S^\alpha_{mj}]. \tag{2.52}$$

Differentiation of Eq. 2.52 with respect to the relative stretch tensor yields

$$\begin{aligned} \mathcal{S}_{ijkl} \doteq\ & R^t_{ik}(t^*)F^e_{lj}(t) - R^t_{ik}(t^*)F^e_{lm}(t)\sum_\alpha \dot{\gamma}^\alpha(t^*)\Delta t S^\alpha_{mj} - \\ & R^t_{in}(t^*)U^t_{np}(t^*)F^e_{pm}(t)\sum_\alpha J^\alpha_{kl}\Delta t S^\alpha_{mj}, \end{aligned} \tag{2.53}$$

where

$$\mathbf{J}^\alpha \equiv \frac{\partial \dot{\gamma}^\alpha(t^*)}{\partial \mathbf{U}^t(t^*)}. \tag{2.54}$$

The partial derivative of the second Piola-Kirchhoff stress with respect to the relative stretch tensor can be found by differentiating Eq. 2.34. The result of that operation is:

$$\mathcal{Q}_{ijkl} = \mathcal{D}_{ijkl} - \Delta t\sum_\alpha C^\alpha_{ij}J^\alpha_{kl} - \Delta t\sum_\alpha \dot{\gamma}^\alpha \mathcal{J}^\alpha_{ijkl}, \tag{2.55}$$

where

$$\mathcal{D}_{ijkl} = \frac{1}{2}\mathcal{L}_{ijmn}\varepsilon_{mnkl}, \tag{2.56}$$

$$\mathcal{J}_{ijkl} = \frac{1}{2}\mathcal{L}_{ijmn}[\varepsilon_{mpkl}S^\alpha_{pn} + \varepsilon_{pnkl}S^\alpha_{pm}], \tag{2.57}$$

with

$$\varepsilon_{ijkl} = F^e_{ki}(t)U^t_{lm}F^e_{mj}(t) + F^e_{mi}(t)U^t_{mk}F^e_{lj}(t). \tag{2.58}$$

To complete the set of equations necessary to determine the material jacobian,

an analytical form for $\mathbf{J}^\alpha$ must be found. The crystallographically-resolved plastic strain rate is a function of the second Piola-Kirchhoff stress and the crystallographic dislocation density state; therefore, $\mathbf{J}^\alpha$ can be written as

$$\begin{aligned} J_{ij}^\alpha &= \frac{\partial \dot{\gamma}^\alpha}{\partial \bar{T}_{kl}} \frac{\partial \bar{T}_{kl}}{\partial U_{ij}^t} + \frac{\partial \dot{\gamma}^\alpha}{\partial \bar{T}_{(cb)kl}} \frac{\partial \bar{T}_{(cb)kl}}{\partial U_{ij}^t} \\ &+ \frac{\partial \dot{\gamma}^\alpha}{\partial \bar{T}_{(pe)kl}} \frac{\partial \bar{T}_{(pe)kl}}{\partial U_{ij}^t} + \frac{\partial \dot{\gamma}^\alpha}{\partial \bar{T}_{(se)kl}} \frac{\partial \bar{T}_{(se)kl}}{\partial U_{ij}^t}. \end{aligned} \tag{2.59}$$

Let

$$M_{kl}^\alpha \equiv \frac{\partial \dot{\gamma}^\alpha}{\partial \bar{T}_{kl}}, \tag{2.60}$$

and

$$N_{ij}^\alpha \equiv \frac{\partial \dot{\gamma}^\alpha}{\partial \bar{T}_{(cb)kl}} \frac{\partial \bar{T}_{(cb)kl}}{\partial U_{ij}^t} + \frac{\partial \dot{\gamma}^\alpha}{\partial \bar{T}_{(pe)kl}} \frac{\partial \bar{T}_{(pe)kl}}{\partial U_{ij}^t} + \frac{\partial \dot{\gamma}^\alpha}{\partial \bar{T}_{(se)kl}} \frac{\partial \bar{T}_{(se)kl}}{\partial U_{ij}^t}, \tag{2.61}$$

Eq 2.59 yields:

$$J_{ij}^\alpha = M_{kl}^\alpha \mathcal{Q}_{klij} + N_{ij}^\alpha. \tag{2.62}$$

Substitution of this result into Eq. 2.55 and solving for $\mathcal{Q}_{ijkl}$ leads to the final expression:

$$\mathcal{Q}_{ijkl} = \left[\delta_{im}\delta_{jn} + \Delta t \sum_\alpha M_{mn}^\alpha C_{ij}^\alpha \right]^{-1} \left[\mathcal{D}_{mnkl} - \Delta t \sum_\alpha N_{mn}^\alpha C_{kl}^\alpha - \Delta t \sum_\alpha \dot{\gamma}^\alpha \mathcal{J}_{mnkl}^\alpha \right]. \tag{2.63}$$

The analytical expression for the material jacobian is an approximate solution, but the level of error is the same as the level of error in calculating the Cauchy stress and the dislocation density state at time t^* as a result of the Taylor expansions that were used to simplify the calculation.

2.2.5 Selection of Material Constants

The fourth-order anisotropic elasticity tensor in the constitutive equation (Eq. 2.6) introduces some elastic constants. At the current stage, the influences of the temperature on the elastic constants are not applied, and the elastic constants are chosen as

[Cuitino and Ortiz, 1993]:

$$C_{11} = 223GPa, \qquad C_{12} = 148GPa, \qquad C_{44} = 125GPa, \tag{2.64}$$

and the shear modulus is given by:

$$\mu = \frac{C_{11} + C_{44} - C_{12}}{3}. \tag{2.65}$$

The constitutive function for the dislocation mobility (Eq. 2.22) also introduced some constants that need to be modeled. Based on the PPV model, Qin and Bassani [1992] deduced the yield criterion for the $L1_2$ intermetallic compounds for each slip system in the following form:

$$\tau^\alpha + A(\tau^\alpha_{pe} - \kappa\tau^\alpha_{se}) + B\tau^\alpha_{cb} = \pm\tau^\alpha_{cr}, \tag{2.66}$$

which is actually in the same form with the contents in the square brackets of Eq. 2.22 if we apply $l \sim 100b$ [Hirsch, 1992] and define:

$$\begin{aligned} A &= \frac{C_2}{300}, \\ B &= \frac{C_3}{300}, \\ \kappa &= \kappa. \end{aligned}$$

As suggested by Qin, the magnitudes of the non-Schmid factors A, B and κ are typically less than unity. The resolved shear stresses of the three vertexes of the spherical triangle for various values of A, B and κ were calculated. And by linear interpolation, the CRSS surfaces over the spherical triangle were created and plotted in Figure 2-6, which have same trend as Bassani's result (shown in Figure 2-5). From the simulation we can see that the degree of the tension-compression asymmetry is controlled by the factor A, and increasing its magnitude produces a larger separation of the tension and compression surfaces. Changing the sign of A exchanges the two surfaces. The factor κ determines the orientations where the CRSS at initial yield in

tension is the same as in compression. The cross-slip factor B influences those crystals oriented near the $[011]-[\bar{1}11]$ boundary. In the simulation, A is chosen to be -0.267, which makes $|\lambda| \sim 10^2$. This is consistent with the magnitude range we deduced for λ in the former section. B is chosen to be -0.1 and $\kappa = 0.5$. $H_{u0}^{\alpha *}$ is considered to be a curve-fitting parameter changing with temperature. In the simulation, the value of $H_{u0}^{\alpha *}$ is estimated to be 1.3, 3.8 and $7.8ev$ for the absolute temperatures of 100, 300 and $500K$, respectively.

2.2.6 Simulation Geometry, Boundary Conditions, and Initial State Conditions

In the simulation of single crystals, the geometry, boundary conditions, and initial state are critical in determining the plastic evolution of the crystal and its state. The simulation geometry used was a unit cube cell, which is assigned to be a brick (C3D8) element as shown in Figure 2-7. General periodic boundary conditions [Danielsson *et al.*, 2002] are imposed on the unit cell. Characteristic points on the surface of the cell are illustrated schematically in Figure 2-7. The relative displacement of node **B** to that of node **A** can be expressed as:

$$\mathbf{u(B)} - \mathbf{u(A)} = \mathbf{u(C)} - \mathbf{u(O)}, \tag{2.67}$$

where $\mathbf{u}$ denotes displacement. A corner point of the unit cell $(\mathbf{O})$ is chosen as a reference point, and its displacement is set to zero; $\mathbf{u(O)} = \mathbf{0}$. The vector between $(\mathbf{O})$ and $(\mathbf{C})$, in the reference configuration is expressed as $\mathbf{p(C)}$. The displacement of $(\mathbf{C})$ can then be expressed in terms of the macroscopic deformation gradient as:

$$\mathbf{u(C)} = (\mathbf{F} - \mathbf{1})\mathbf{p(C)}. \tag{2.68}$$

Upon combining Eq. 2.67 and Eq. 2.68, we arrive at the periodic boundary condition:

$$\mathbf{u(B)} - \mathbf{u(A)} = (\mathbf{F} - \mathbf{1})\mathbf{p(C)} \tag{2.69}$$

To simulate the boundary condition of uniaxial tension with constant strain rate, some d.o.f.s of certain nodes are predescribed by adding constraints to the components of the macroscopic deformation gradient:

$$F_{12} = F_{13} = F_{23} = 0$$

$$F_{33} = 1 + \Delta t \dot{\epsilon}_{app}$$

where $\dot{\epsilon}_{app}$ is the applied constant strain rate (in the small strain range).

In order to predict the dependence of yield stresses on different orientations and compare with the experimental results quoted by Vitek [Vitek and Pope, 1984], four particular crystallographic orientations were chosen for simulation. The Euler angles related to these four orientations can be found in Figure 2-8. A summary description of Euler angles, Miller Indices, and stereographic projection is presented in Appendix A.

2.2.7 Results and Discussion

The simulation results of tensile and compressive yield strengths at fixed temperature, for the four chosen orientations, are shown in Figures 2-9 through 2-12, and also in Tables 2-3 and 2-4. Temperatures of 100, 300 and $500K$ were selected for each case, and a strain rate of $|\dot{\epsilon}_{app}| = 1.3 \times 10^{-3} s^{-1}$ was applied.

The simulations reasonably capture the principal character of the yield behavior of Ni_3Al:

1. The simulation successfully presents the anomalous yield property of Ni_3Al under the peak temperature ($\sim 800K$). The yield stress increases with increasing temperature for all orientations, both in tension and compression.

2. The simulation shows a reasonable tension-compression asymmetry of the yield stress for all orientations. For case A, which is actually the $< 001 >$ orientation, the yield stress in tension is always higher than in compression. In case

B, tension-compression asymmetry is hardly observed. While for other cases, compression is always higher. For each orientation, the difference of yield stress between tension and compression also increases with increasing temperature, which matches the testing result quite well.

3. A strain rate sensitivity study was undertaken in the $< 001 >$ direction for both tension and compression. Strain rates of $1.0 \times 10^{-3} s^{-1}$ and $1.0 \times 10^{-4} s^{-1}$ were applied to each case, and the simulation results are shown in Figure 2-13. The change in strain rate of 10 times hardly affects the yield stress, in agreement with experimental observations.

From the simulation results, we find that the strain-stress curve becomes completely flat after the yield point. Such a non-hardening character has its origins in the steady-state assumption of Hirsch's model. As mentioned in Chapter 1, high strain hardening rate has been reported in $L1_2$ structure compounds, which also shows unusual relations with temperature in the yield anomalous region. Thus, Hirsch's superkink model needs some adjustments to give a better prediction of the deformation properties of $L1_2$ alloys. In the next chapter, some ideas are proposed for revising the current model.

(a)

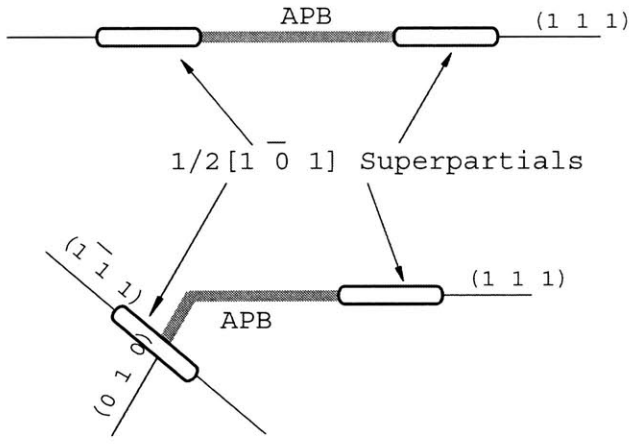

(b)

Figure 2-1: (a) Structure of dissociated dislocation in Ni_3Al, (b) Process of core transformation.

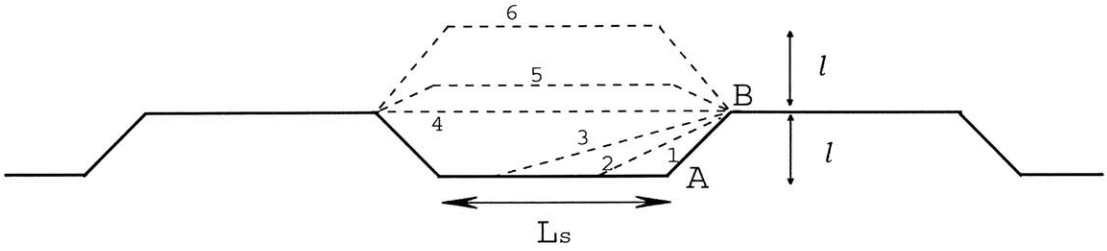

(a)

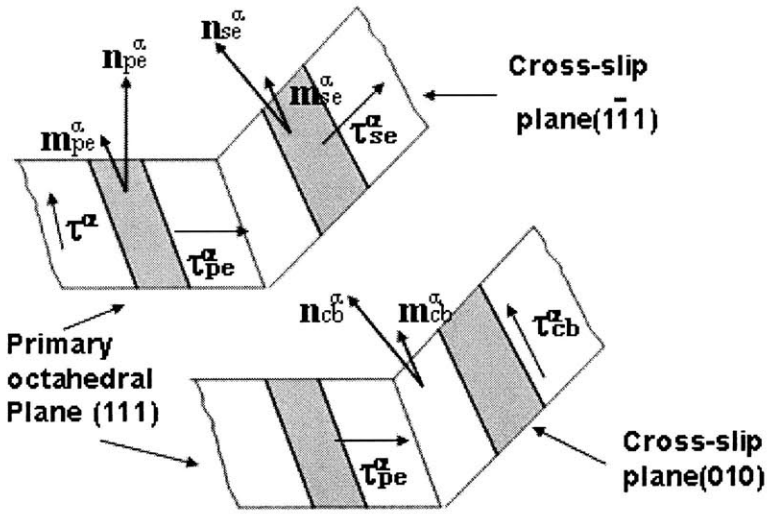

(b)

Figure 2-2: (a) Steady-state configuration for unlocking-locking sequence [Hirsch, 1992]; (b) Non-Schmid stress components [Allan, 1995].

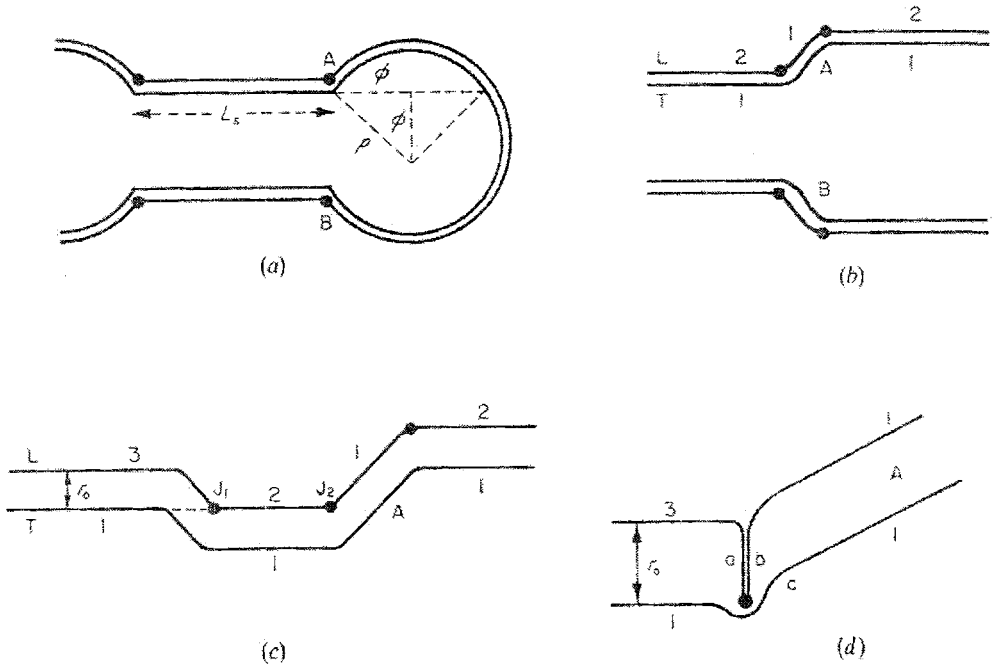

Figure 2-3: Formation of edge dislocation dipole barriers; (111) planes at different levels are indicated by numbers; the original glide plane is marked by 1, 2, and 3 correspond to levels $w = b/2$ and b below plane 1. (a) A screw segment with length of L_s cross-slipped; (b) Formation of superkinks (marked with A and B) with further movement of the edge-orientated dislocation; (c) A second cross-slip; (d) Formation of the dipole barriers [Hirsch, 1992].

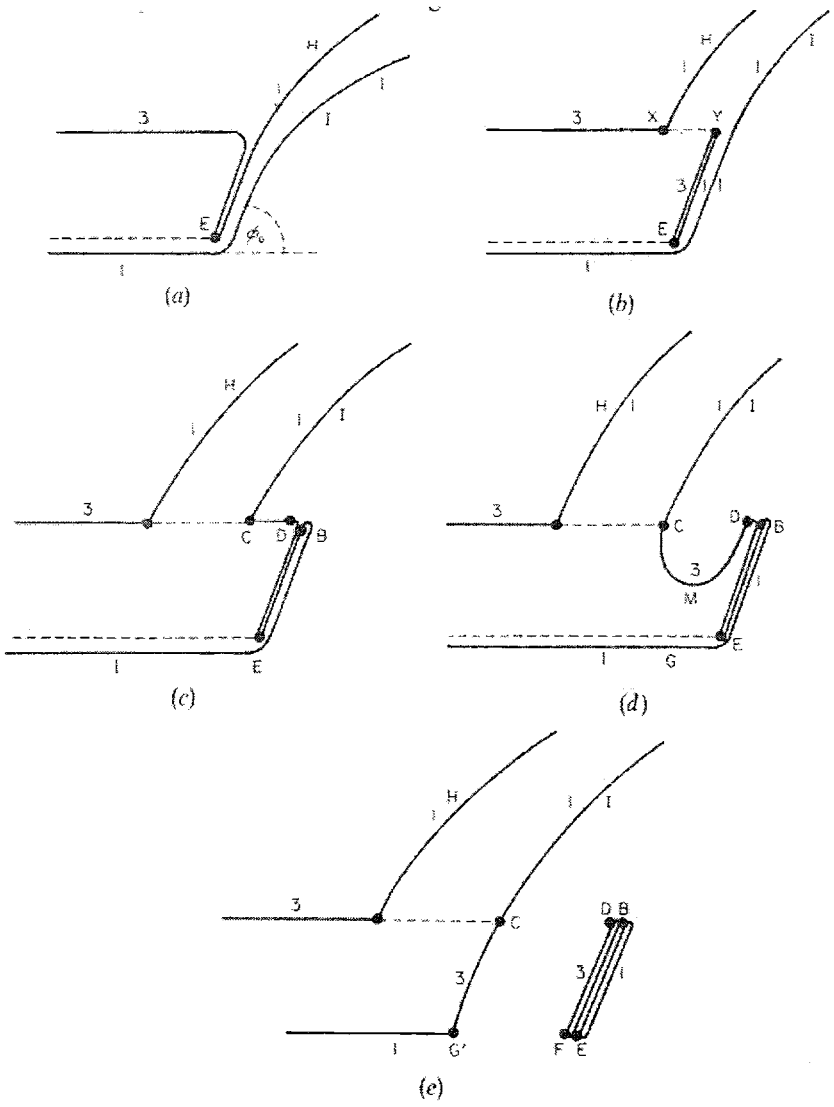

Figure 2-4: Bypassing of dipole by superkink; numbers indicate different levels of (111) planes with the numbering scheme as in Figure 2-3 [Hirsch, 1992].

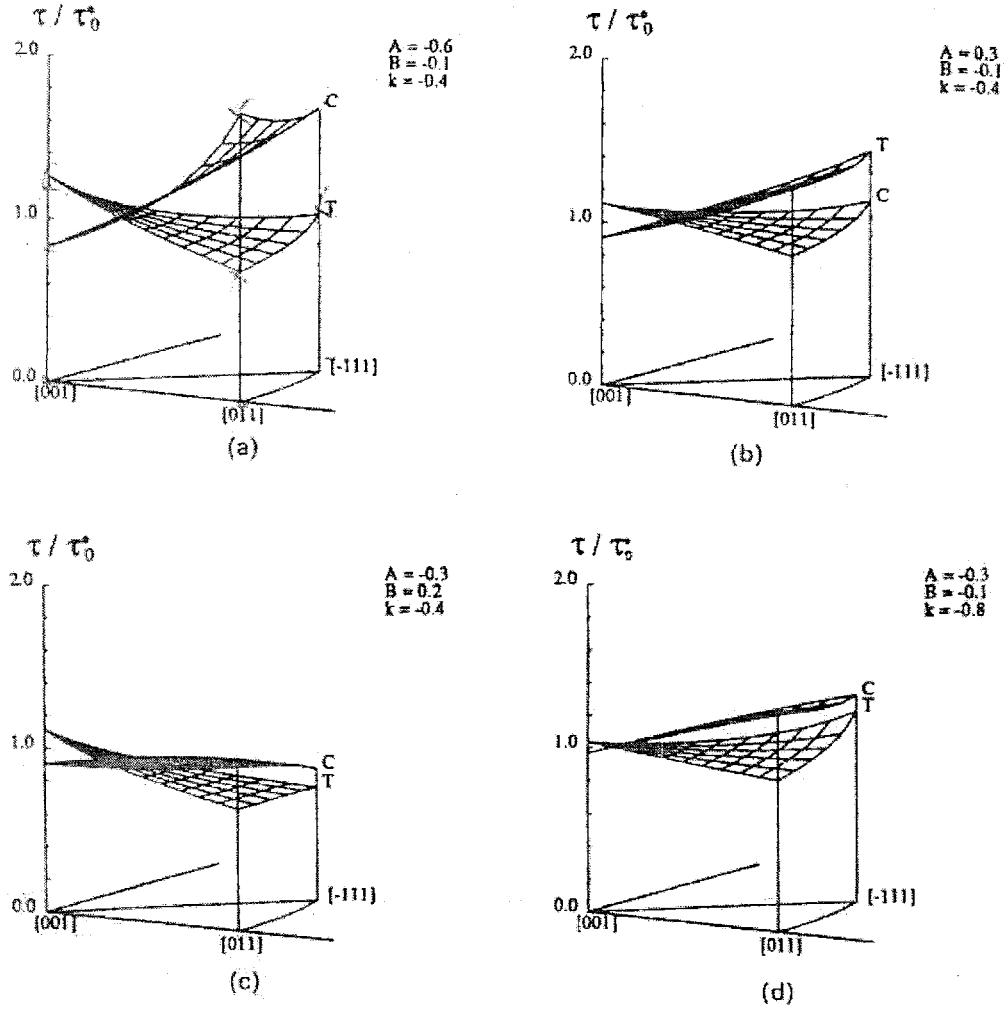

Figure 2-5: Prediction of effects of non-Schmid factors by Bassani [1994].

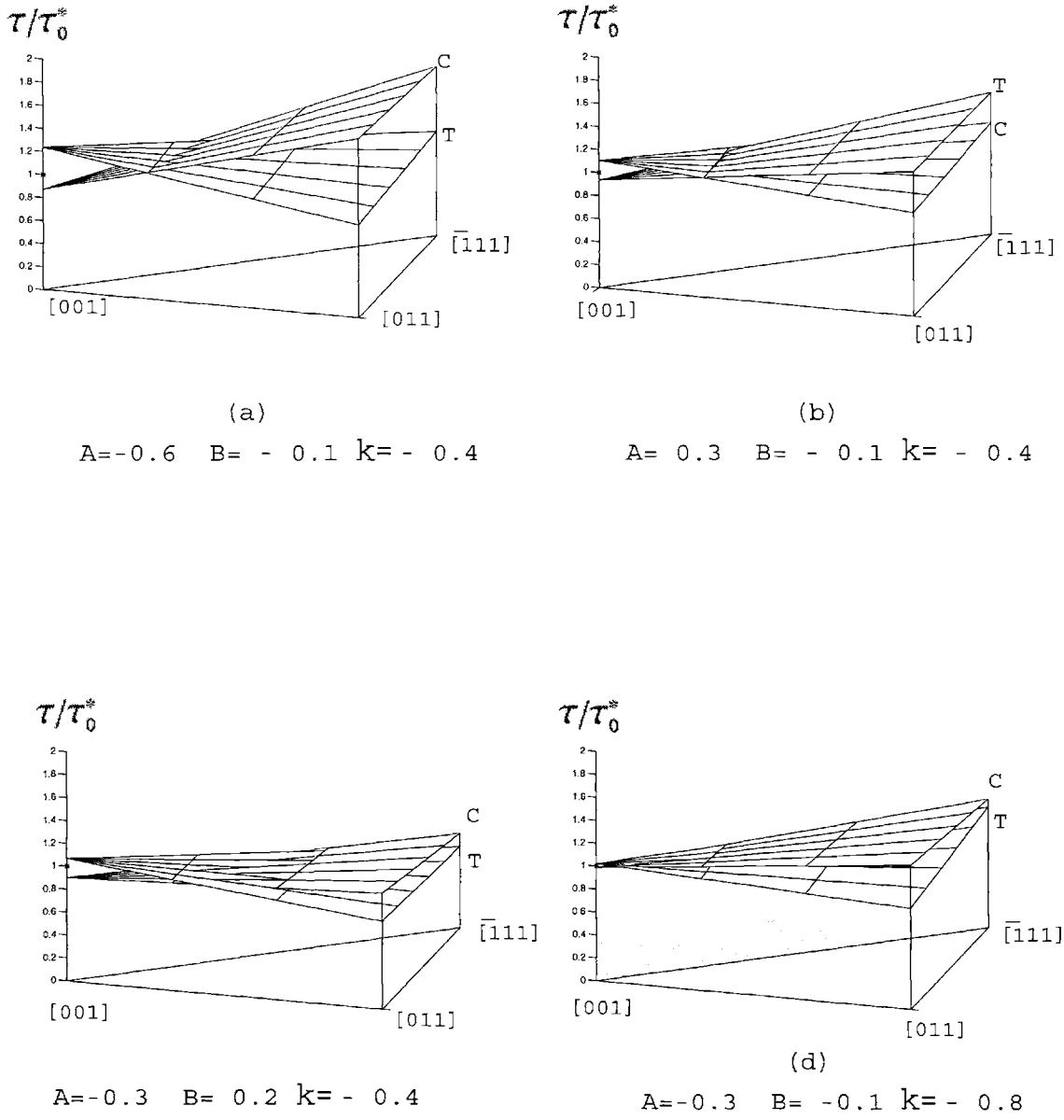

Figure 2-6: Simulation result: Parameter study of non-Schmid factors.

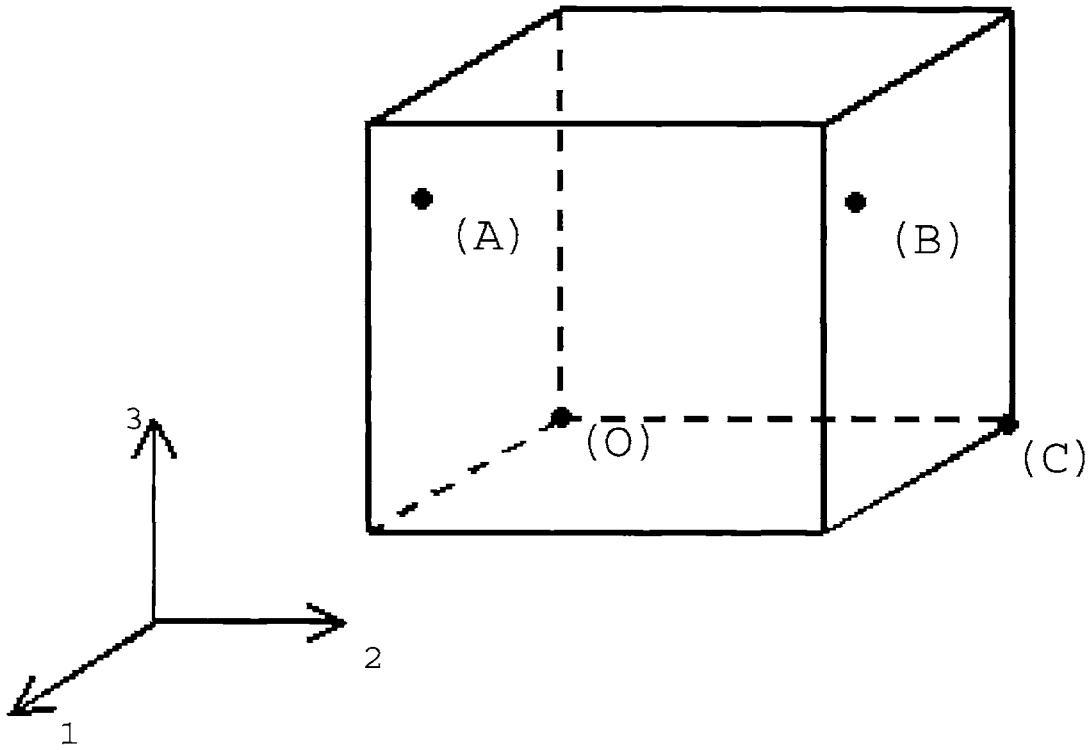

Figure 2-7: Simulation Geometry.

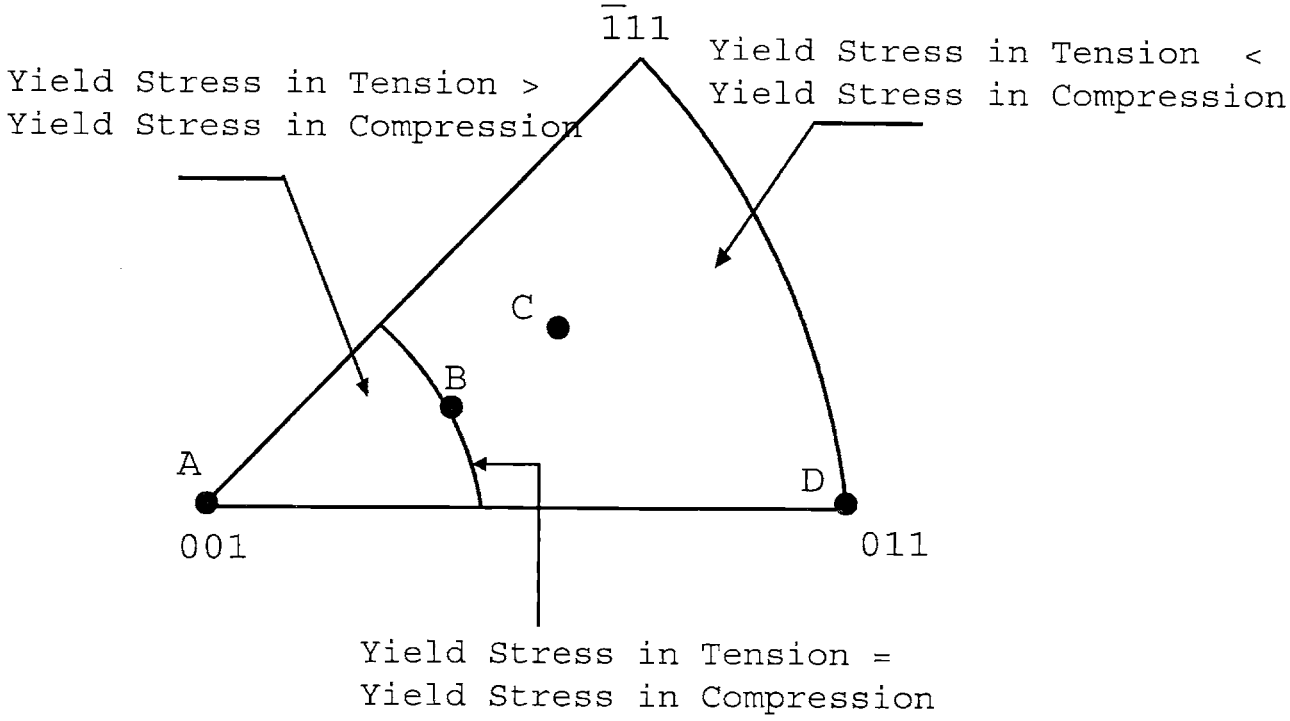

(a)

case #	Euler Angles		
	θ (°)	ϕ (°)	ω (°)
A	0	0	0
B	-20.14	23.26	0
C	-33.09	27.26	0
D	-45	0	0

(b)

Figure 2-8: Descriptions of the four orientations selected in the simulation: (a) in the unit stereographic triangle; (b) with Euler angles.

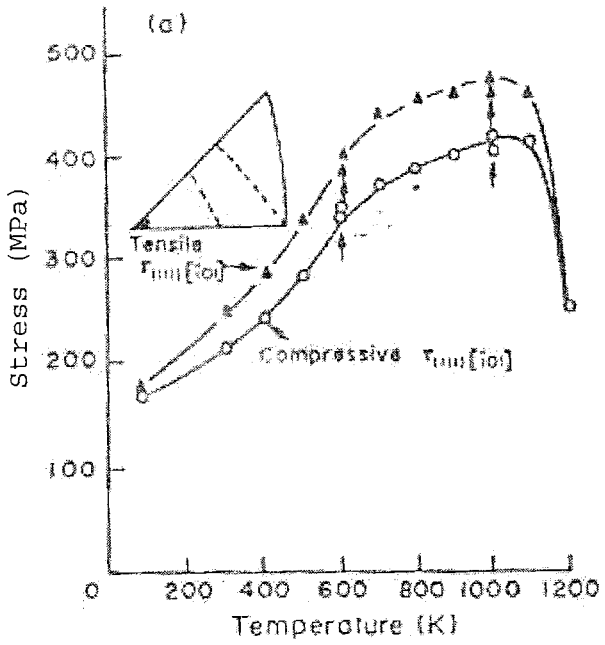

(a)

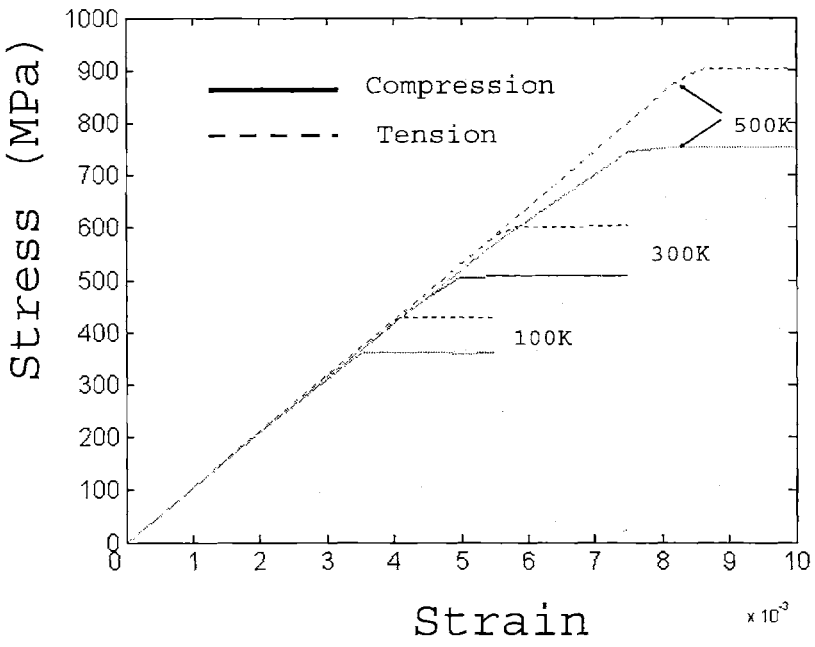

(b)

Figure 2-9: Uniaxial stressing simulation (Case 1): (a) Experimental results (CRSS) [Umakoshi et al.,1984]; (b) Simulation results (uniaxial stress).

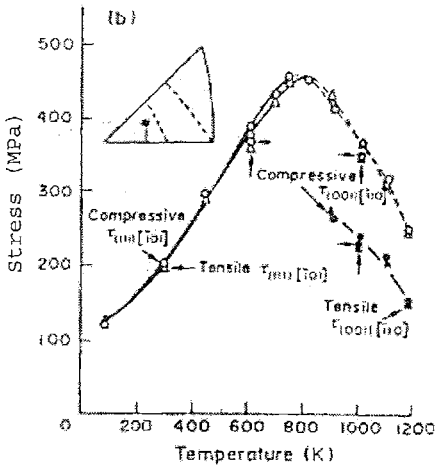

(a)

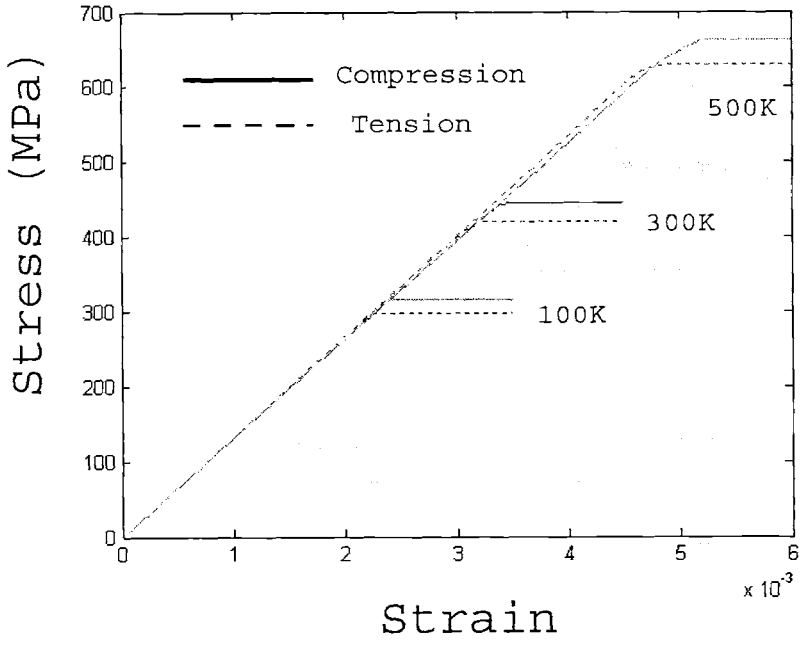

(b)

Figure 2-10: Uniaxial stressing simulation (Case 2): (a) Experimental results (CRSS) [Umakoshi et al.,1984]; (b) Simulation results (uniaxial stress).

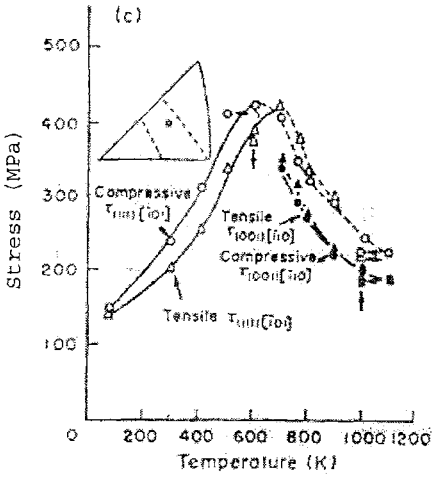

(a)

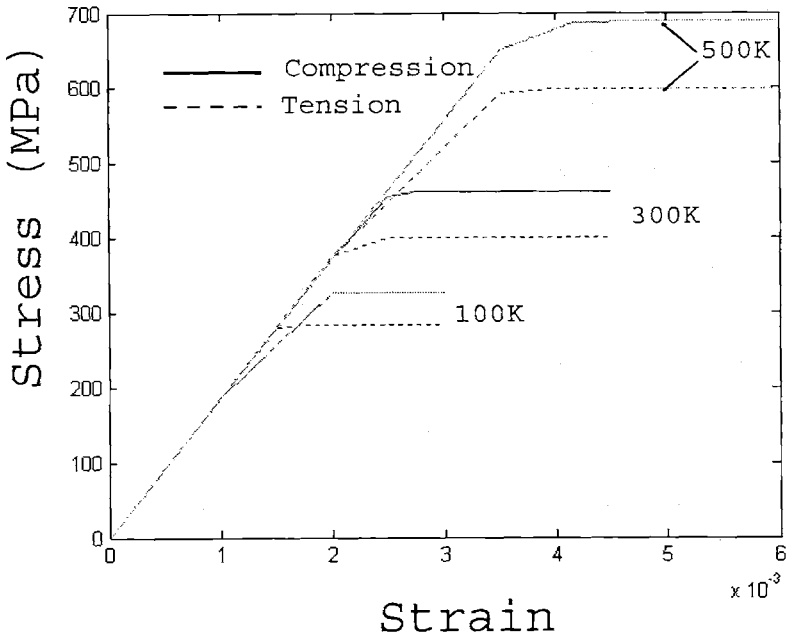

(b)

Figure 2-11: Uniaxial stressing simulation (Case 3): (a) Experimental results (CRSS) [Umakoshi et al.,1984]; (b) Simulation results (uniaxial stress).

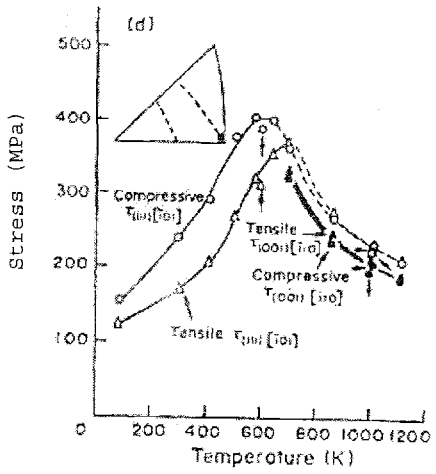

(a)

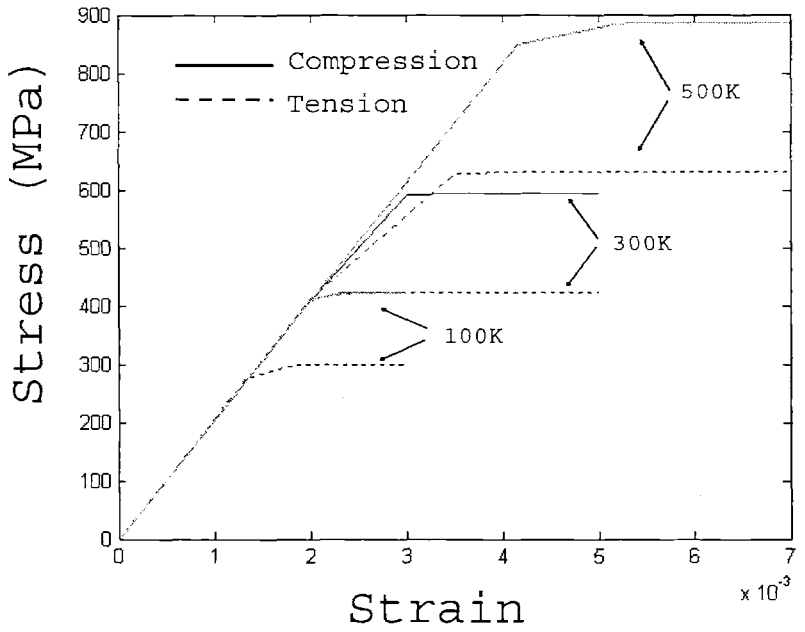

(b)

Figure 2-12: Uniaxial stressing simulation (Case 4): (a) Experimental results (CRSS) [Umakoshi et al.,1984]; (b) Simulation results (uniaxial stress).

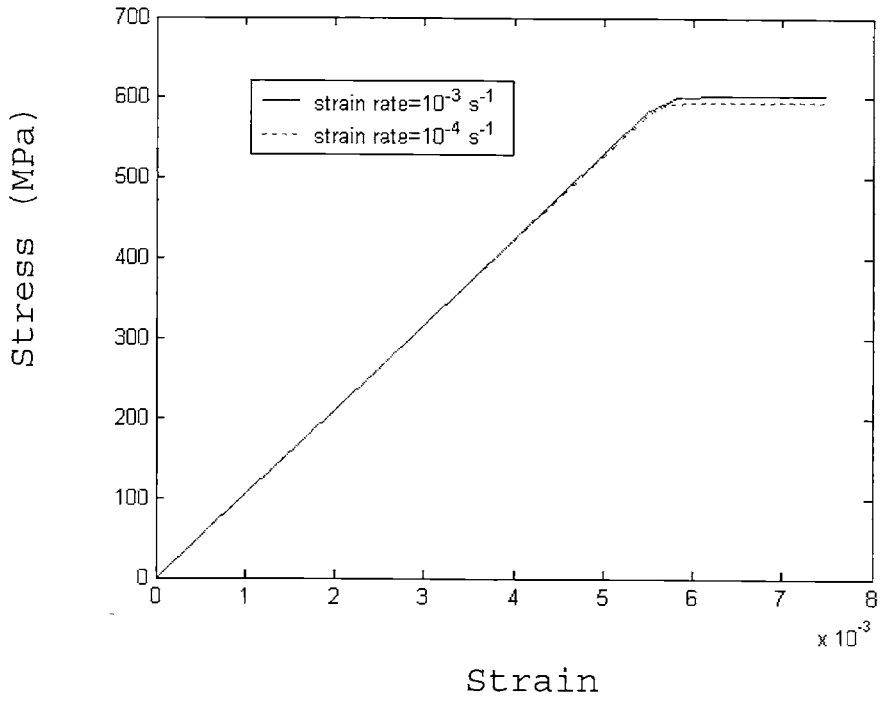

Figure 2-13: Study of strain rate sensitivity: Simulation of uniaxial tension in $\langle 001 \rangle$ direction, at 300K with different strain rates.

Table 2.1: The dislocation basis used in the simulation.

ρ Index	**b**	**t**	**n**
1	$[1\bar{1}0]$	$[1\bar{1}0]$	$[111]$
2	$[\bar{1}01]$	$[\bar{1}01]$	$[111]$
3	$[01\bar{1}]$	$[01\bar{1}]$	$[111]$
4	$[110]$	$[110]$	$[1\bar{1}\bar{1}]$
5	$[\bar{1}0\bar{1}]$	$[\bar{1}0\bar{1}]$	$[1\bar{1}\bar{1}]$
6	$[0\bar{1}1]$	$[0\bar{1}1]$	$[1\bar{1}\bar{1}]$
7	$[\bar{1}\bar{1}0]$	$[\bar{1}\bar{1}0]$	$[\bar{1}1\bar{1}]$
8	$[10\bar{1}]$	$[10\bar{1}]$	$[\bar{1}1\bar{1}]$
9	$[011]$	$[011]$	$[\bar{1}1\bar{1}]$
10	$[\bar{1}10]$	$[\bar{1}10]$	$[\bar{1}\bar{1}1]$
11	$[101]$	$[101]$	$[\bar{1}\bar{1}1]$
12	$[0\bar{1}\bar{1}]$	$[0\bar{1}\bar{1}]$	$[\bar{1}\bar{1}1]$

Table 2.2: The octahedral slip systems.

α	$(\mathbf{n}^\alpha)[\mathbf{m}^\alpha]$	$(\mathbf{n}^\alpha_{pe})[\mathbf{m}^\alpha_{pe}]$	$(\mathbf{n}^\alpha_{se})[\mathbf{m}^\alpha_{se}]$	$(\mathbf{n}^\alpha_{cb})[\mathbf{m}^\alpha_{cb}]$
1	$(111)[1\bar{1}0]$	$(111)[11\bar{2}]$	$(\bar{1}\bar{1}1)[\bar{1}\bar{1}\bar{2}]$	$(100)[01\bar{1}]$
2	$(111)[\bar{1}01]$	$(111)[1\bar{2}1]$	$(\bar{1}1\bar{1})[\bar{1}\bar{2}\bar{1}]$	$(010)[\bar{1}01]$
3	$(111)[01\bar{1}]$	$(111)[\bar{2}11]$	$(1\bar{1}\bar{1})[\bar{2}\bar{1}\bar{1}]$	$(001)[1\bar{1}0]$
4	$(1\bar{1}\bar{1})[110]$	$(1\bar{1}\bar{1})[1\bar{1}2]$	$(\bar{1}1\bar{1})[\bar{1}12]$	$(100)[0\bar{1}1]$
5	$(1\bar{1}\bar{1})[\bar{1}0\bar{1}]$	$(1\bar{1}\bar{1})[12\bar{1}]$	$(\bar{1}\bar{1}1)[\bar{1}21]$	$(0\bar{1}0)[\bar{1}0\bar{1}]$
6	$(1\bar{1}\bar{1})[0\bar{1}1]$	$(1\bar{1}\bar{1})[\bar{2}\bar{1}\bar{1}]$	$(111)[\bar{2}11]$	$(00\bar{1})[110]$
7	$(\bar{1}1\bar{1})[\bar{1}\bar{1}0]$	$(\bar{1}1\bar{1})[\bar{1}12]$	$(1\bar{1}\bar{1})[1\bar{1}2]$	$(\bar{1}00)[011]$
8	$(\bar{1}1\bar{1})[10\bar{1}]$	$(\bar{1}1\bar{1})[\bar{1}2\bar{1}]$	$(111)[1\bar{2}1]$	$(010)[10\bar{1}]$
9	$(\bar{1}1\bar{1})[011]$	$(\bar{1}1\bar{1})[21\bar{1}]$	$(\bar{1}\bar{1}1)[2\bar{1}1]$	$(00\bar{1})[\bar{1}\bar{1}0]$
10	$(\bar{1}\bar{1}1)[\bar{1}10]$	$(\bar{1}\bar{1}1)[\bar{1}\bar{1}2]$	$(111)[11\bar{2}]$	$(\bar{1}00)[0\bar{1}\bar{1}]$
11	$(\bar{1}\bar{1}1)[101]$	$(\bar{1}\bar{1}1)[\bar{1}21]$	$(1\bar{1}\bar{1})[12\bar{1}]$	$(0\bar{1}0)[101]$
12	$(\bar{1}\bar{1}1)[0\bar{1}\bar{1}]$	$(\bar{1}\bar{1}1)[2\bar{1}1]$	$(\bar{1}1\bar{1})[21\bar{1}]$	$(001)[\bar{1}10]$

Table 2.3: Comparison of testing and simulation results: Yield stress.

Case Number (θ, ϕ, ω)		100 K		300 K		500 K	
		Expt.	Sim.	Expt.	Sim.	Expt.	Sim.
A	$\lvert\sigma_y\rvert_C$(MPa)	416	360	526	507	710	753
(0,0,0)	$\lvert\sigma_y\rvert_T$(MPa)	445	427	612	602	820	893
B	$\lvert\sigma_y\rvert_C$(MPa)	262	315	413	445	631	662
(-20.14,23.63,0)	$\lvert\sigma_y\rvert_T$(MPa)	250	297	397	420	615	630
C	$\lvert\sigma_y\rvert_C$(MPa)	308	327	493	461	776	688
(-33.09,27.26,0)	$\lvert\sigma_y\rvert_T$(MPa)	283	283	419	400	650	600
D	$\lvert\sigma_y\rvert_C$(MPa)	374	421	588	593	882	885
(-45,0,0)	$\lvert\sigma_y\rvert_T$(MPa)	296	299	416	422	661	630

Table 2.4: Comparison of testing and simulation results: Tension-compression asymmetry.

Case Number		100 K		300 K		500 K	
		Expt.	Sim.	Expt.	Sim.	Expt.	Sim.
A	$(\lvert\sigma_y\rvert_C$-$\lvert\sigma_y\rvert_T)$(MPa)	-29	-67	-85	-95	-110	-150
B	$(\lvert\sigma_y\rvert_C$-$\lvert\sigma_y\rvert_T)$(MPa)	12	18	16	25	20	32
C	$(\lvert\sigma_y\rvert_C$-$\lvert\sigma_y\rvert_T)$(MPa)	25	44	73	61	126	89
D	$(\lvert\sigma_y\rvert_C$-$\lvert\sigma_y\rvert_T)$(MPa)	78	122	171	171	220	255

Chapter 3

A revised dynamical-superkink model

The $L1_2$ intermetallic compounds were originally chosen as the focus of intensive research because of the discovery of their anomalous temperature dependence of the yield stress. It might be for this reason that most of the existing theories (both qualitative and quantitative) have emphasized the modeling of "yielding". Hirsch's superkink model, which has been particularly mentioned in Chapter 2, provides a successful explanation for almost all yield properties about the $L1_2$ intermetallic compounds. Meanwhile, such a model, which simulates the motion of the screw dislocation by a steady-state approach, is destined to a non-hardening prediction after the yield point. An important aspect of deformation properties of the $L1_2$ compounds, however, is that the work hardening rate (WHR) at any given strain also exhibits an unusual behavior in the anomalous regime and can reach astonishingly large values. Nevertheless, the peak stress temperature is observed to be higher than the peak WHR temperature (Figure 3-1).

The high rate of strain hardening which is intrinsic to the motion of dislocations, forces us to reconsider the validity of the steady-state assumption. In a reliable model, yielding and strain hardening should be reflections of the same dislocation dynamics so that they can be naturally connected.

3.1 Evolution of Mobile Dislocation Density and Superkink Height

To the author's knowledge, no systematic theory has been developed for strain hardening in $L1_2$ alloys. The following model is a revision of the superkink locking-unlocking model, based on the experimental observation of superkink height evolution.

A statistical analysis of superkink-height distribution was performed by Couret, Sun, and Hirsch [1993]. Single crystals of Ni_3Ga alloys were deformed in compression at different temperatures with a constant strain rate of $10^{-4}\ s^{-1}$. Weak-beam TEM was used to measure the superkink heights in Ni_3Ga at $\epsilon \sim 2\%$ (ϵ is the engineering strain). Experimental results give an exponential distribution as shown in Figures 3-2 and 3-3, which can be expressed in the following way:

$$N(l^* - \frac{\Delta l}{2} \leq l \leq l^* + \frac{\Delta l}{2}) = N_0 \exp(-\frac{l^*}{l_0}), \tag{3.1}$$

where l^* is the sample dislocation height, N_0 is a constant, $N(l^*)$ is the number of superkinks (per unit volume) with height l ($l \subset [l^* - \frac{\Delta l}{2}, l^* + \frac{\Delta l}{2}]$). The value for Δl is given to be $5nm$ in this statistical analysis. l_0 is a distribution variable ($l_0 = 13nm$ at $293K$ and $l_0 = 9nm$ at $673K$). Hence, statistically, the superkink distribution function can be defined as:

$$N(l_1 \leq l \leq l_2) = \int_{l_1}^{l_2} \frac{N_0}{\Delta l} \exp(-\frac{l}{l_0})\, dl, \tag{3.2}$$

Based on the experimental observation of superkink distribution, we assume that not all superkinks are mobile. Rather, only those whose heights are larger than a critical value (under a certain applied stress), can unlock the K-W locks and move as described in Hirsch's model. This feature is similar to one made by Louchet in the ELU model [Louchet, 1995]. Since the eventual movement of the screw dislocations is due to the superkinks shuttling on them, the mobility of the screw is then connected to its superkink heights. Screws with longer kinks are more mobile than those with

shorter ones, and when the superkink height on a screw dislocation segment is below the critical value, the screw is assumed to be exhausted or immobile.

In this way, the screw dislocation density is decomposed into two parts, a mobile one and an immobile one. Instead of a constant value of total screw dislocation density (in Hirsch's model), the mobile screw dislocation density, which changes with applied stress, deformation and temperature, is applied to calculate the plastic strain rate.

3.2 Description of the dynamical-superkink model

The form of superkink distribution raises doubts about simulating the dislocation mobility by one screw dislocation having superkinks with a constant height (as used in Hirsch's model). An alternative model involving multi-screws has been applied and schematically shown in Figure 3-4 (b). For simplicity, the height of the superkinks on each screw is assumed to be the same, but differs for different screws, and the distribution of the height satisfies the exponential form. In this way, the screw dislocation density distribution is connected with the kink height and has the same exponential form:

$$\rho(l_1 \leq l \leq l_2) = \int_{l_1}^{l_2} \frac{\rho_0}{\Delta l} \exp(-\frac{l}{l_0})\, dl, \tag{3.3}$$

If we make an assumption that the total screw dislocation density is constant, the mobile dislocation density for the slip system α can be deduced in the following way:

$$\frac{{\rho_m}^{\alpha}}{{\rho_{total}}^{\alpha}} = \frac{\int_{l_c^{\alpha}}^{l_{max}} \frac{\rho_0}{\Delta l} \exp(-\frac{l}{l_0^{\alpha}})\, dl}{\int_0^{l_{max}} \frac{\rho_0}{\Delta l} \exp(-\frac{l}{l_0^{\alpha}})}, \tag{3.4}$$

$${\rho_m}^{\alpha} = \rho_{total}^{\alpha} \left[\frac{exp(-\frac{{l_c}^{\alpha}}{{l_0}^{\alpha}}) - exp(-\frac{l_{max}}{{l_0}^{\alpha}})}{1 - exp(-\frac{l_{max}}{{l_0}^{\alpha}})}\right]. \tag{3.5}$$

where l_{max} is the maximum value of superkink height, and ${l_c}^{\alpha}$ is the critical superkink height for the slip system α, which is given as:

$$
\begin{aligned}
{l_c}^{\alpha} &= C\frac{b\mu}{\tau^{\alpha}} \qquad (\text{if} \quad {l_c}^{\alpha} \leq l_{max}); \\
{l_c}^{\alpha} &= l_{max} \qquad (\text{if} \quad {l_c}^{\alpha} > l_{max}),
\end{aligned} \tag{3.6}
$$

in which, C is a dimensionless constant of order 10^{-1}, b is the length of Burgers vector, μ is the shear modulus, and τ^{α} is the applied stress for each slip system.

Each individual screw dislocation in this multi-screw model still moves by switching between the locked phase and the unlocked phase, similar to the single-screw model described by Hirsch. However, the superkink height of each screw does change, reflected by a variation of the kink height distribution. In the calculation the screw velocity, the constant superkink height that appeared in Eq. 2.20 should be modified as the average height of the mobile kinks, given by the following form:

$$
\begin{aligned}
\bar{l}^{\alpha} &= \frac{(l_c^{\alpha} + l_0^{\alpha})\exp(-\frac{l_c^{\alpha}}{l_0^{\alpha}}) - (l_{max}^{\alpha} + l_0^{\alpha})\exp(-\frac{l_{max}^{\alpha}}{l_0^{\alpha}})}{1 - \exp(-\frac{l_{max}^{\alpha}}{l_0^{\alpha}})} \qquad (\text{if} \quad {l_c}^{\alpha} \leq l_{max}); \\
\bar{l}^{\alpha} &= l_{max}^{\alpha} \qquad (\text{if} \quad {l_c}^{\alpha} > l_{max}).
\end{aligned} \tag{3.7}
$$

Since ${l_c}^{\alpha}$ is a function of applied stress, the average superkink height is thus a function of τ and l_0. The evolution of the kink height distribution variable l_0 needs to be defined to close this modeling framework.

Many factors influence the kink height distribution. Since the kink height is assumed to be the same as the average advance distance of screw segment between two successive locking configurations, the kink height should be affected by the locking frequency, and the screw velocity between two successive locking phases. On the other hand, the kink height distribution also changes with the dynamical evolution of the kinks themselves, mainly by the interactions of superkinks with both different and same signs, which overall tends to decrease the population of longer kinks but to generate more shorter ones.

Based on the above analysis, the distribution variable l_0, is considered to be a func-

tion of temperature, applied stress and the mobile dislocation density. A definition in rate form is given as:

$$\dot{l}_0^\alpha = -B_1(l_0^\alpha - l_{ss}^\alpha(\theta)) - B_2 l_0^\alpha \dot{\gamma}^\alpha. \tag{3.8}$$

The first part on the right side represents the trend to reach a steady-state value, l_{ss}^α , while the second part accounts for the evolution of superkinks. B_1, and B_2 are two dimensionless constants. Considering the experimental results, the initial value of the l_0 is given as a monotone decreasing function of temperature.

$\bar{l}$ has been defined as a function of $l_c(t^*)$ and l_0 in Eq. 3.7, and Figure 3-5 schematically shows the influence of applied shear stress and the kink height distribution variable l_0 on $\bar{l}$. With both increasing τ and decreasing l_0, $\bar{l}$ decreases. Since the core part of the revised model is the connection of the average superkink height, $\bar{l}$, with the mobility of the screw dislocation, under constant strain rate conditions, such a decrease of the average kink height requires a significant increase in the applied stress, which explains the high rate of strain hardening phenomena.

Simulation results based on the above model are shown in Figure 3-6. Even though the revised model has not been completely calibrated, the simulation does give promising results, showing both the anomalous increase of yield stress with increasing temperature, and a reasonably high value of strain hardening rate. The revised model is also able to predict the tension-compression asymmetry and orientation dependence of the yield stress, since it inherits the non-Schmid stress effect from the original model.

3.3 Future Work

As the most important strengthening constituent in commercial nickel-based superalloys, the $L1_2$ structure compounds Ni_3Al have been investigated frequently in the last several decades. Nonetheless, no existing theories can explain the unusual mechanical behaviors of $L1_2$ structure compounds completely.

The dynamical superkink model discussed in this chapter is basically a revised

version of Hirsch's superkink locking-unlocking model by introducing the assumption of exhaustion of screw dislocations in a way similar to that presented by Chrzan and Mills [Chrzan and Mills, 1996]. Though the simulation results seems to be promising, the model has not been completed yet, and an abundance of work based on a better understanding of the physical background needs to be done in order to give better predictions for both yielding and strain hardening properties of the $L1_2$ structure compounds:

Firstly, the evolution of the superkink distribution parameter l_0 needs to be carefully modeled, because it greatly influences the change of the average superkink height, which determines the mobility of the screw dislocation. In the current rate-form definition, the value of the steady-state part, l_{ss}^{α}, has not been explicitly defined. If chosen as a constant for a given temperature, a reasonable prediction of strain hardening rate can be achieved, remaining almost constant after yield point and differing for different crystal orientations, which is consistent with the experimental results. But this model as outlined does not work so well in predicting the anomalous increase of the WHR with temperature till a peak WHR temperature, which is lower than the peak yield temperature.

Secondly, terms other than those explicitly involved the resolved shear stresses in calculating the locking and unlocking enthalpy are essentially treated as disposable curve-fitting constants. Actually, some of them theoretically depend on the micromechanics and the APB energies. How these terms change with temperature, and applied stress is not yet very clear.

Finally, the assumption that the total screw dislocation density maintains as a constant may need to be reconsidered. A recent study by Kruml *et al.* [2001] in $Ni_3(Al, 3.3\%Hf)$ single crystal at $373K$ shows that an increase of 150% of the total screw dislocation density after 1% resolved plastic strain.

How the above issues ultimately affect the simulations needs to be carefully examined. After consummation, this model could then be incorporated into a modeling framework for simulating the mechanical behavior of nickel-based superalloys.

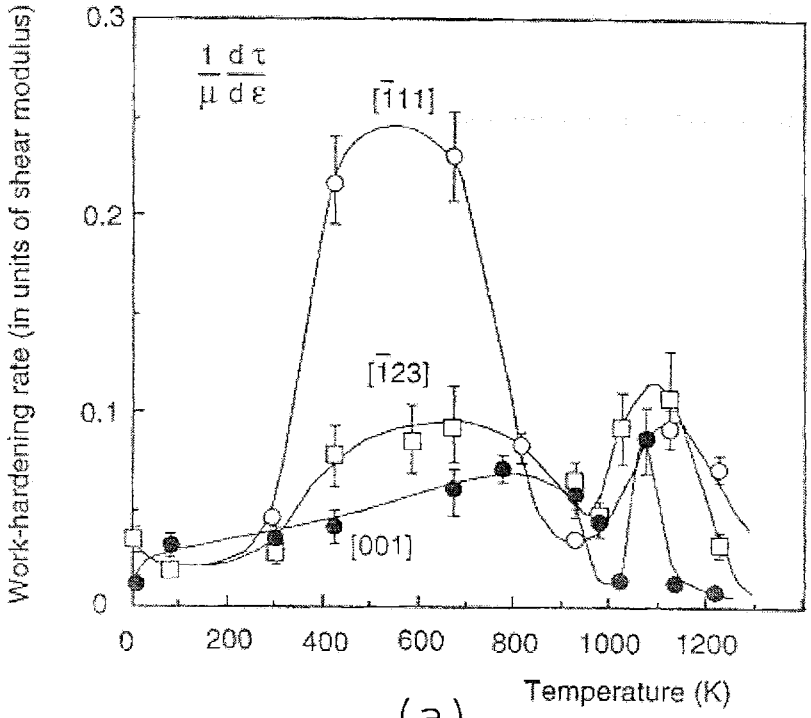

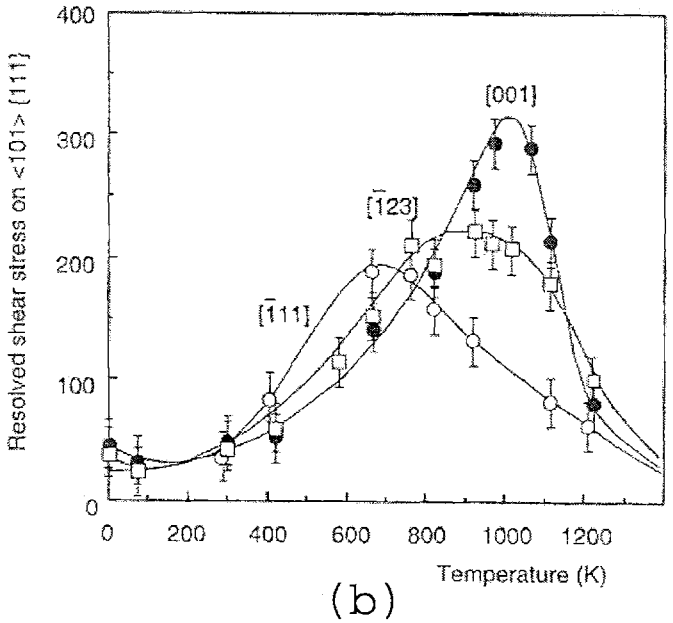

Figure 3-1: $Ni_3(Al, 0.25at.\%Hf)$ deformed in compression. Temperature and orientation dependence of (a) the work-hardening rate, and (b) the 0.2% shear stress in MPa [Staton-Bevan, 1983].

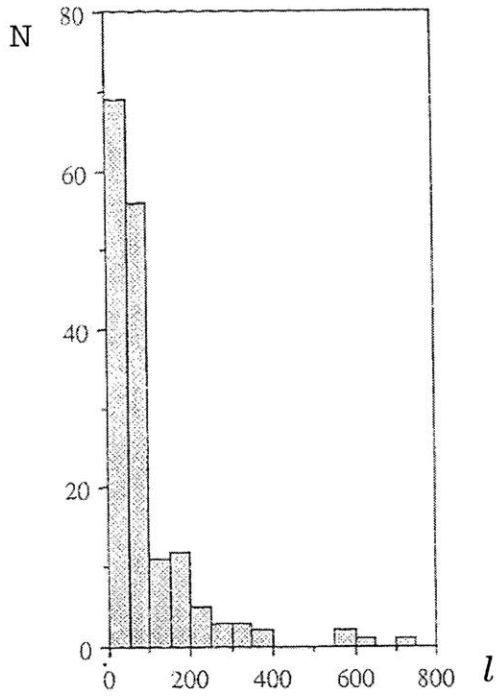

Figure 3-2: Superkink height measurements at 400^oC, where l is the superkink height (in $\mathring{A}$) and N is the number of superkinks having a height l, (a) plot on a linear scale; (b) plot on a semi-logarithmic scale [Couret, *et al.*, 1993].

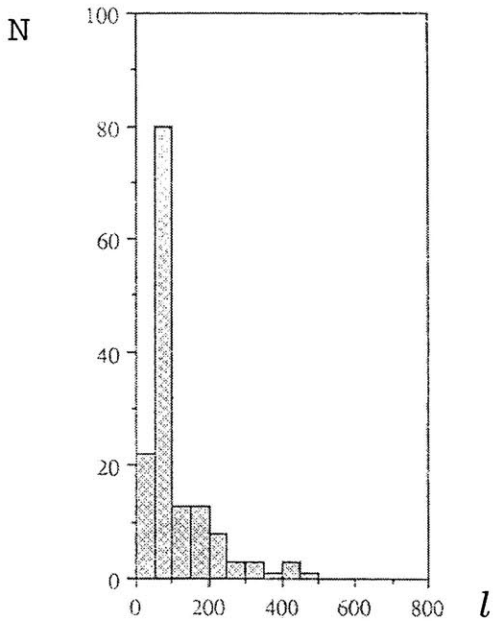

(a)

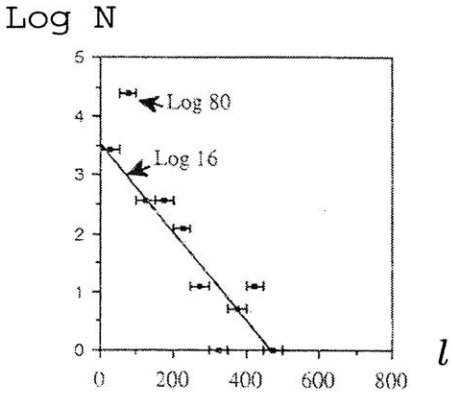

(b)

Figure 3-3: Superkink height measurements at $20°C$, where l is the superkink height (in $\mathring{A}$) and N is the number of superkinks having a height l, (a) plot on a linear scale; (b) plot on a semi-logarithmic scale [Couret, *et al.*, 1993].

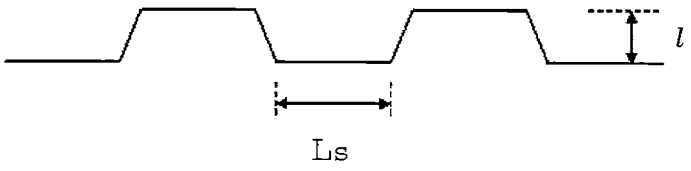

(a)

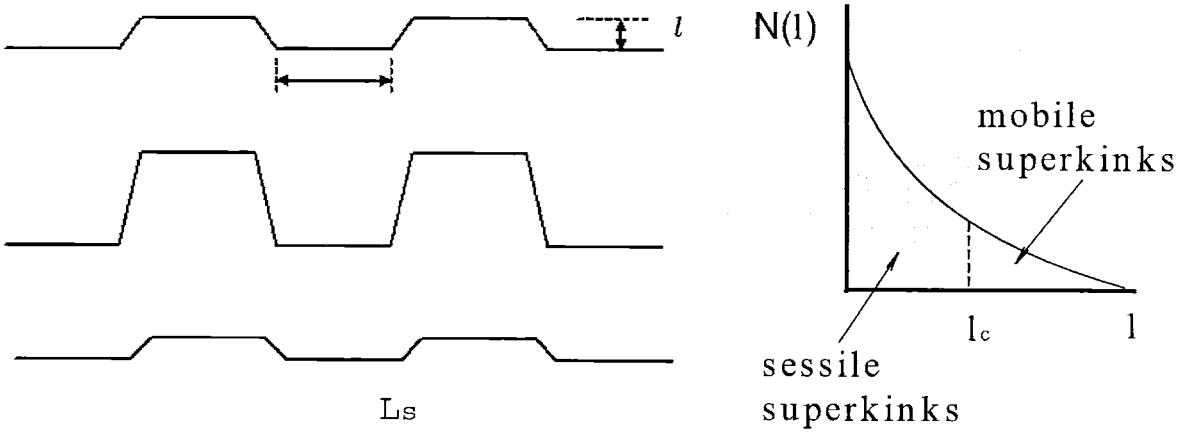

Figure 3-4: Illustration of the (a) Hirsch's single-superkink model; (b) Revised multi-superkink model. The height of superkinks differs for different screw dislocations, and has an exponential-form distribution.

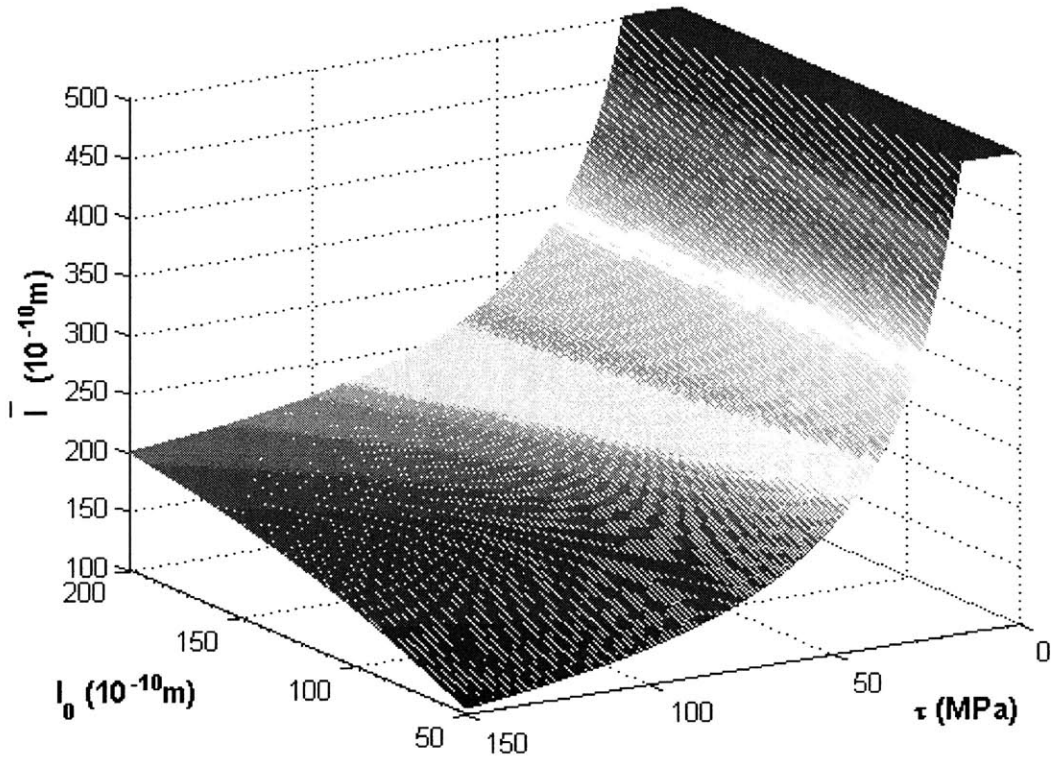

Figure 3-5: The influence of the applied stress and the kink height distribution variable on the average kink height.

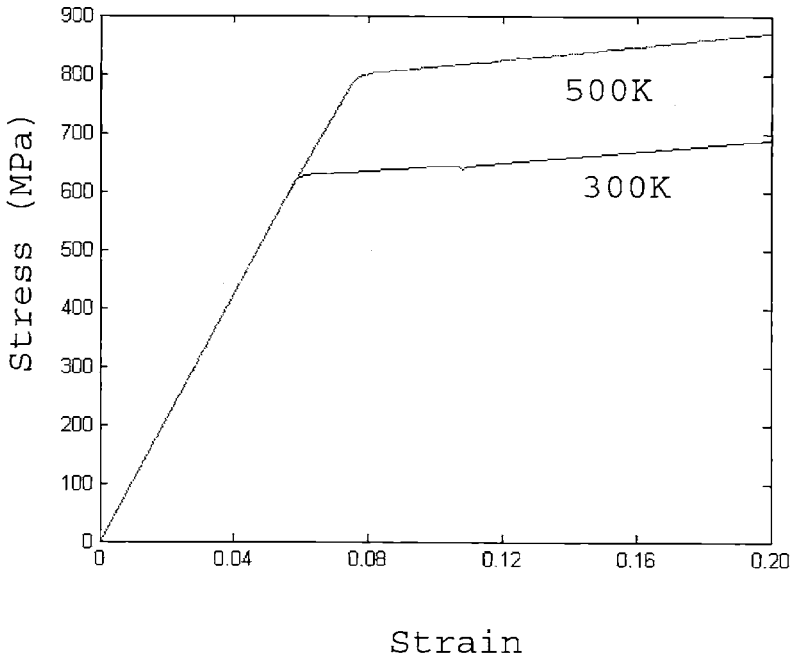

Figure 3-6: Simulation result by the revised model.

Appendix A

Definition and Determination of Crystal Orientations

A.1 Miller Indices

A crystal direction is usually given by Miller Indices. Miller Indices are a symbolic vector representation for the orientation of an atomic plane in a crystal lattice and are defined as the reciprocals of the fractional intercepts, which the plane makes with the crystallographic axes. These indicies, (hkl) (in parentheses), define the orientation of a plane or, equivalently, the normal to that plane, $[hkl]$ (in square brackets) [Whittaker, 1981].

A.2 Euler Angles

Many material properties, elastic constants, for example, are given in tensor form. These tensors are usually given in a basis of crystal orientations (the crystal coordinate system). While the deformation tensors are usually given in a global coordinate system (Figure (A-1 (a)). Thus, transformations between the global coordinates and the crystal coordinates are necessary and are defined by a set of Euler angles. According to Euler's rotation theorem, any rotation may be described using three angles (ϕ, θ, ω), as shown in Figure (A-1 (b)). The superscript "g" represents global

system, and "c" represents the crystal system. The procedure in going from the basis $\mathbf{e}^c$ to the basis $\mathbf{e}^g$ is as follows:

1. Rotate by an angle ϕ around the c-axis. The result is $a \rightarrow a'$ and $b \rightarrow b'$.

2. Rotate by an angle θ around the a'-axis. The result is $b' \rightarrow b''$ and $c \rightarrow c'$ (or $\mathbf{e}_3^g$).

3. Rotate by an angle ω around the c'-axis. The result is $b'' \rightarrow b'''$ (or $\mathbf{e}_2^g$) and $a' \rightarrow a''$ (or $\mathbf{e}_1^g$).

The three rotations can be written in terms of the following matrices:

$$\mathbf{Q}_\phi = \begin{bmatrix} \cos\phi & \sin\phi & 0 \\ -\sin\phi & \cos\phi & 0 \\ 0 & 0 & 1 \end{bmatrix} \tag{A.1}$$

$$\mathbf{Q}_\theta = \begin{bmatrix} 1 & 0 & 0 \\ 0 & \cos\theta & \sin\theta \\ 0 & -\sin\theta & \cos\theta \end{bmatrix} \tag{A.2}$$

$$\mathbf{Q}_\omega = \begin{bmatrix} \cos\omega & \sin\omega & 0 \\ -\sin\omega & \cos\omega & 0 \\ 0 & 0 & 1 \end{bmatrix} \tag{A.3}$$

Hence , the total rotation from the crystal to the global orientation, $\mathbf{Q}$, is given by:

$$\begin{aligned} \mathbf{Q} &= \mathbf{Q}_\phi \mathbf{Q}_\theta \mathbf{Q}_\omega \\ &= \begin{bmatrix} \cos\phi\cos\omega - \sin\phi\sin\omega\cos\theta & \sin\phi\cos\omega + \cos\phi\sin\omega\cos\theta & \sin\omega\sin\theta \\ -\cos\phi\sin\omega - \sin\phi\cos\omega\cos\theta & -\sin\phi\sin\omega + \cos\phi\cos\omega\cos\theta & \cos\omega\sin\phi \\ \sin\phi\sin\theta & -\cos\phi\sin\theta & \cos\theta \end{bmatrix} \end{aligned}$$

A.3 Stereographic projection

The stereographic projection is a projection of points from the surface of a sphere on to a projection plane. The procedure of the projection is schematically shown in Figure A-2. If any point P on the surface of the sphere is joined to the point of projection B and the line PB cuts the projection plane at P', then P' is the stereographic projection of P. The importance of the stereographic projection in crystallography is that it preserves the angular relationships between the crystal planes.

Figure A-3(a) shows the [001] projection. The subset of those orientations which are unique is contained in a unit stereographic triangle with corners at the [001], [011] and [$\bar{1}$11] orientations, as shown in Figure A-3 (b) ([Cullity, 1978]).

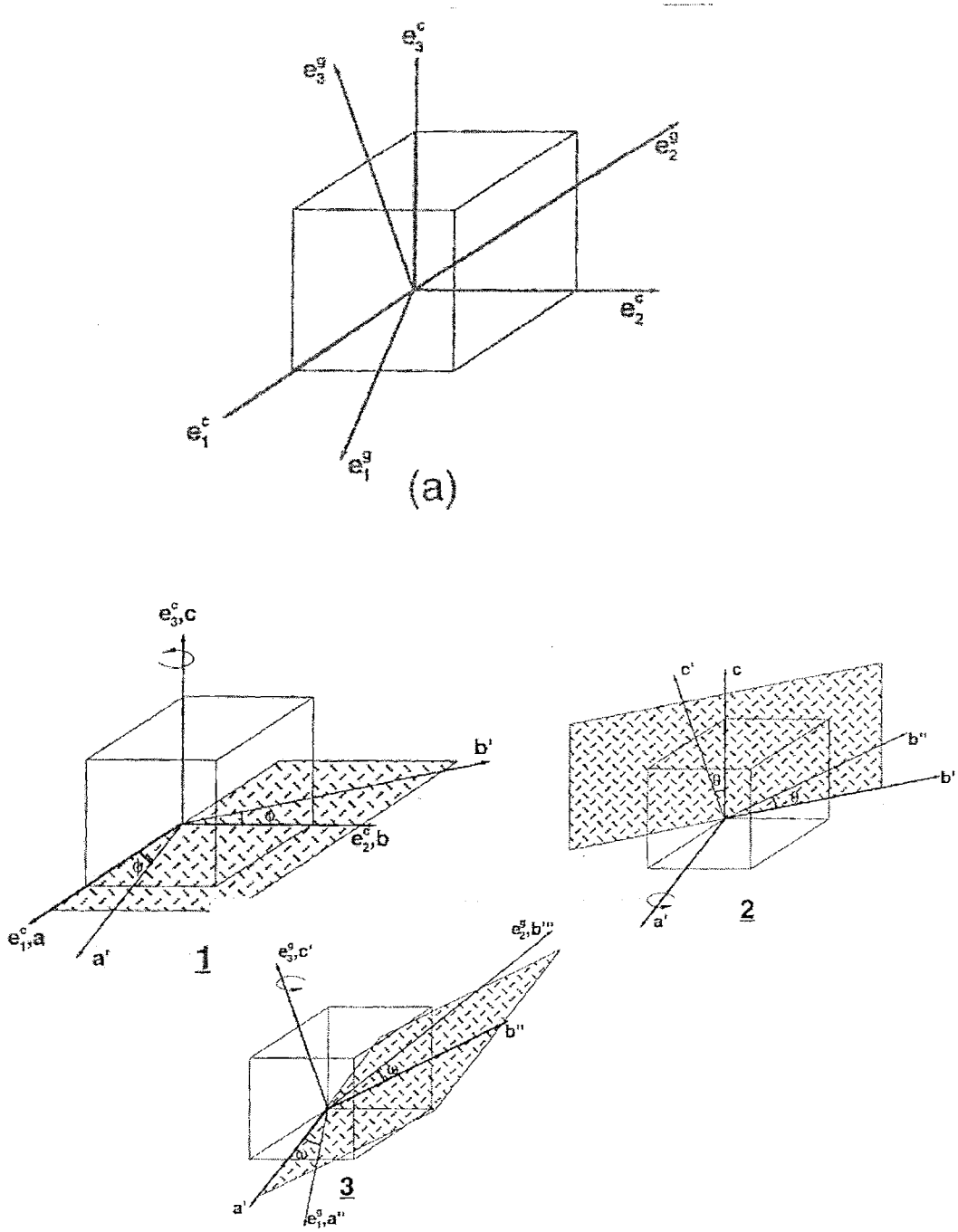

Figure A-1: (a) Definition of global coordinate system with respect to crystal coordinate system. (b) Definition of Euler angles. [Allan,1995]

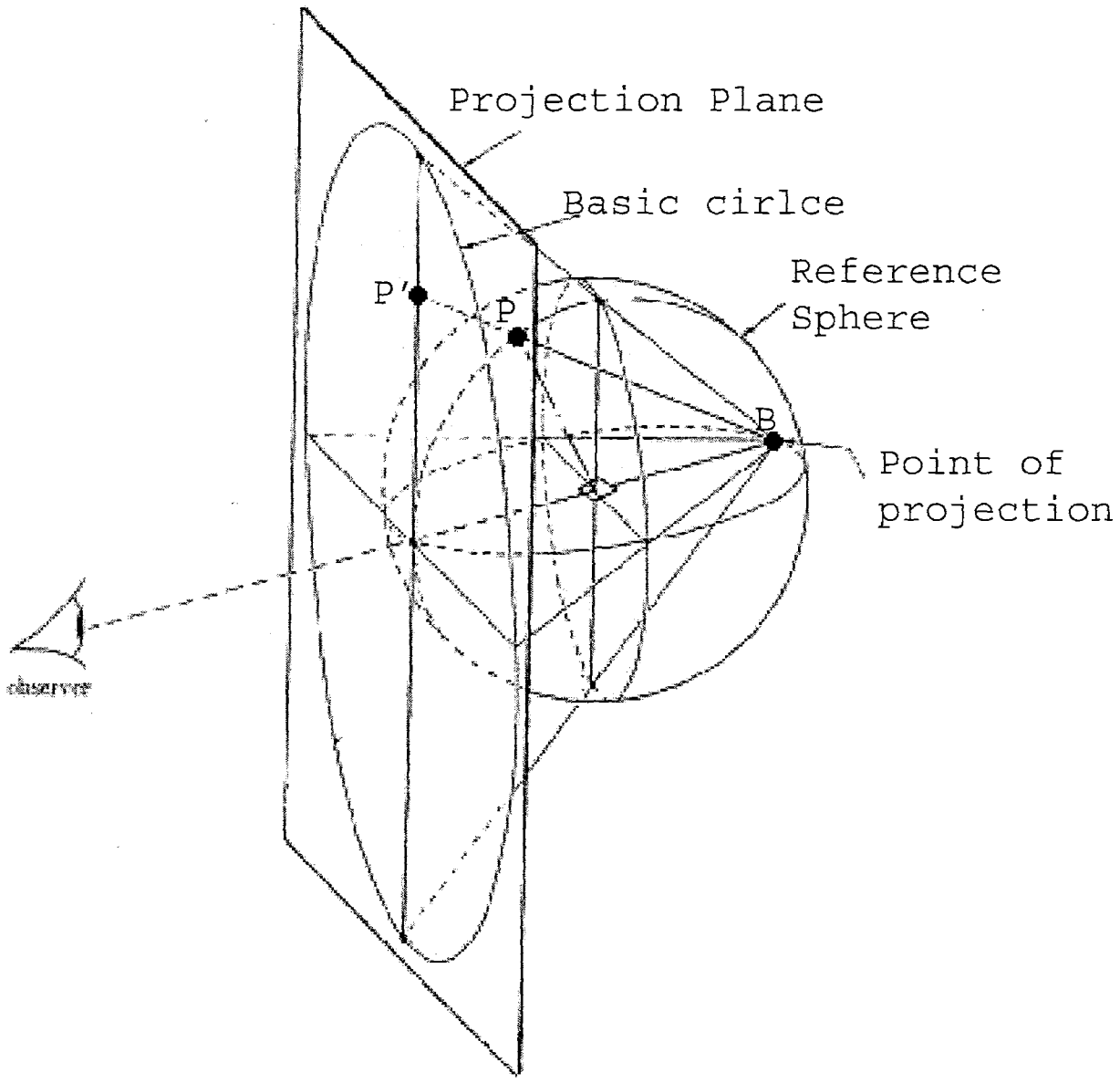

Figure A-2: Formation of stereographic projection [Cullity, 1978]

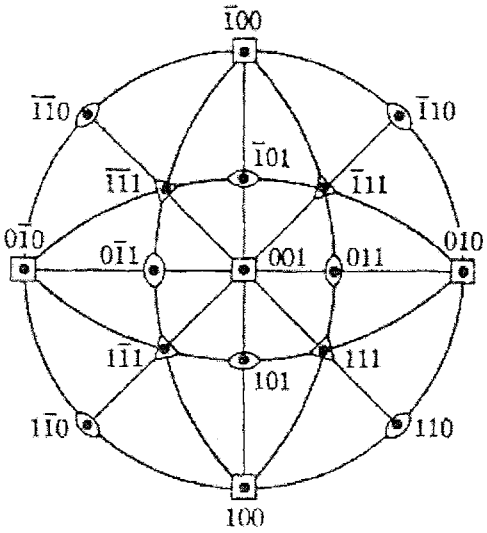

(a)

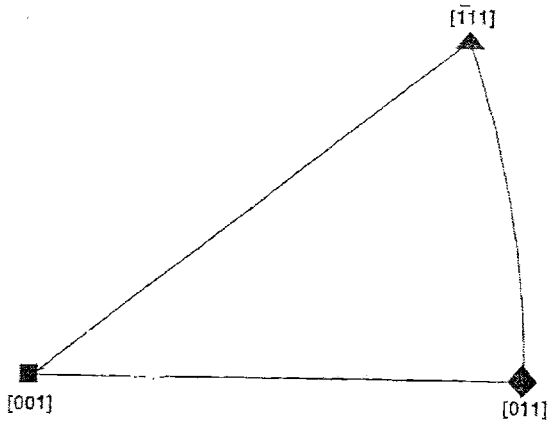

(b)

Figure A-3: (a) [001] Stereographic projection [Cullity, 1978]; (b) Unit stereographic triangle

Bibliography

[1] Allan D.C., (1995), Plasticity of nickel based single crystal superalloys, PhD Thesis, MIT.

[2] Arsenlis, A. (2001), Modeling Dislocation Density Evolution in Continuum Crystal Plasticity, PhD Thesis, MIT.

[3] Asaro R. J. and Rice J. R (1977), Strain localization in ductile single crystals. *J. mech. Phys. Solids*, V25: 309.

[4] Bontemps C. (1991), Thesis, University of Orsay, France. (cited by Caillard and Couret, 1996)

[5] Brown N.(1959), *Phil. Mag. A*, V4: 185.

[6] Caillard D., Clenment N. and Couret A. (1998), *Phil. Mag. Lett.*, V58: 263

[7] Caillard D. and Couret A. (1996), Dislocation Cores and Yield Stress Anomalies, *Dislocations in Solids*, V10: 69.

[8] Couret A., Sun Y.Q. and Hirsch P.B. (1993), *Phil. Mag. A*, V164: 407.

[9] Cuitino A.M. and Ortiz M. (1993), *Mater. Sci. Eng.* V170: 111.

[10] Cullity B.D. (1978), *Elements of X-Ray Diffraction.*, Addison-Wesley Publishing Co.

[11] Danielsson M., Parks D.M., Boyce M.C. (2002), *J. Mech Phys. Solids*, V50(2): 351.

[12] Dimiduk D. (1989), PhD Thesis, Carnegie Mellon University. (cited by Caillard and Couret, 1996)

[13] Ezz S.S., Pope D.P. and Paidar V. (1982), *Acta Metall. Mater.*, V30: 921.

[14] Ezz S.S. and Hirsch P.B. (1995), High-Temperature Ordered Intermetallic Alloys, *MRS Symp. Proc.*, V364: 35.

[15] Flinn P.A. (1960). Theory of Deformation in Superlattices. *Trans. AIME*, V218:145

[16] Frost H.J. and Ashby M.F.(1971), *J. Appl. Phys.*, V42: 5273.

[17] Hirsch P. B. (1992), A new theory of the anomalous yield stress in $L1_2$ alloys, *Phil. Mag. A*, V65: 569

[18] Kear B. H. and Hornbecher M. F (1966), *Trans. ASM*, V59: 155.

[19] Kear B. H. and Wilsdorf G. F. (1962), *Trans. TMS-AIME* , V224: 382.

[20] Kruml T., Martin J.L., Paidar V. (2001), Structural Intermetallics, *The Minerals, Metals and Materials Society, Warrendale, PA* , 457.

[21] Lall C., Chin S. and Pope D.P. (1979), *Metall. Trans. A*, V10: 1323.

[22] Liu C.T. and Pope D.P.(1994), *Intermetallic compounds*, V2: 17.

[23] Louchet F.(1995), *Journal de Physique III*, V5: 1803.

[24] Lours P., Coujou A. and Coulomb P. (1991), *Acta Metall.*, V39: 1787.

[25] Mills M.J. and Chrzan D.C.(1992), *Acta Metall. Mater.*,V40:3051.

[26] Molenat G., Caillard D., Sun Y.Q. and Couret A. (1993), *Mater. Sci. Eng. A*, V164:407.

[27] Molenat G., Caillard D (1994), *Phil. Mag. A*, V69: 939.

[28] Mulford R.A. and Pope D.P. (1973), *Acta Metall.*, V21: 1375.

[29] Nemoto M., Echigoya J. and Suto H. (1977), *Japan Soc. Of Electron Microscopy*, 467.

[30] Paidar B. ,Pope D.P. and Vitek V. (1984), *Acta Metall. Mater*, V32: 435.

[31] Qin Q., and Bassani J.L. (1992), *J. Mech. Phys. Solids*, V40: 813.

[32] Saada G. and Veyssiere P. (1993), *Structural Intermetallics, TMS Publ.*, 379.

[33] Schmid E. (1924), *Appl. Mech., Delft.*, 342.

[34] Staton-Bevan A.E. (1983), *Phil. Mag. A*, V47: 939.

[35] Staton-Bevan A.E. and Rawlings R.D. (1975), *Phil. Mag.*, V32: 787.

[36] Sun Y.Q. (1995), *MRS Bull.*, V20(7): 29.

[37] Sun Y.Q. and Hazzledine P. M. (1988), *Phil. Mag. A*, V58: 603.

[38] Takeuchi S. and Kuramoto E. (1971), *J. Phys. Soc.*, V31: 1282.

[39] Takeuchi S. and Kuramoto E. (1973), *Acta Metall.*, V21: 415.

[40] Thornton P.H., Davies R.G. and Johnston T. L. (1970), *Metall. Trans. A*, V1: 207.

[41] Umakoshi Y., Pope D.P and Vitek V. (1984), *Acta Metall.*, V32: 449.

[42] Westbrook J.H.(1957), Temperature Dependence of the Hardness of Secondary Phases Common in Turbine Bucket Alloys. *Trans. AIME*, V209: 898.

[43] Whittaker, E.J. (1981), Crystallography, Published Oxford ; New York : Pergamon Press .

[44] Veyssiere P. (1989), *MRS Symp. Proc.*, V133: 175.

[45] Vitek V. and Pope D.P. (1996), *Dislocations in Solids*, V10: 135.

[46] Yoo M.H. (1986), *Scripta Metall. Mater.*, V20: 915.